

REPORT DOCUMENTATION PAGE					<i>Form Approved OMB No. 0704-0188</i>	
<small>The public reporting burden for this collection of information is estimated to average 1 hour per response, including the time for reviewing instructions, searching existing data sources, gathering and maintaining the data needed, and completing and reviewing the collection of information. Send comments regarding this burden estimate or any other aspect of this collection of information, including suggestions for reducing the burden, to Department of Defense, Washington Headquarters Services, Directorate for Information Operations and Reports (0704-0188), 1215 Jefferson Davis Highway, Suite 1204, Arlington, VA 22202-4302. Respondents should be aware that notwithstanding any other provision of law, no person shall be subject to any penalty for failing to comply with a collection of information if it does not display a currently valid OMB control number.</small>						
PLEASE DO NOT RETURN YOUR FORM TO THE ABOVE ADDRESS.						
1. REPORT DATE (DD-MM-YYYY)		2. REPORT TYPE			3. DATES COVERED (From - To)	
4. TITLE AND SUBTITLE				5a. CONTRACT NUMBER		
				5b. GRANT NUMBER		
				5c. PROGRAM ELEMENT NUMBER		
6. AUTHOR(S)				5d. PROJECT NUMBER		
				5e. TASK NUMBER		
				5f. WORK UNIT NUMBER		
7. PERFORMING ORGANIZATION NAME(S) AND ADDRESS(ES)					8. PERFORMING ORGANIZATION REPORT NUMBER	
9. SPONSORING/MONITORING AGENCY NAME(S) AND ADDRESS(ES)					10. SPONSOR/MONITOR'S ACRONYM(S)	
					11. SPONSOR/MONITOR'S REPORT NUMBER(S)	
12. DISTRIBUTION/AVAILABILITY STATEMENT						
13. SUPPLEMENTARY NOTES						
14. ABSTRACT						
15. SUBJECT TERMS						
16. SECURITY CLASSIFICATION OF:			17. LIMITATION OF ABSTRACT	18. NUMBER OF PAGES	19a. NAME OF RESPONSIBLE PERSON	
a. REPORT	b. ABSTRACT	c. THIS PAGE			19b. TELEPHONE NUMBER (Include area code)	

Center for Advanced Sensors

Final Report 2005 Funding

Period of Performance 31 March 2005 – 31 August 2006

US Army Contract W911NF-05-2-0019

Dr. Carl Halford, Director

Center for Advanced Sensors

The University of Memphis

Memphis, Tennessee 38152-3180

1.0 Center for Advanced Sensors

1.1 Administrative

This report covers the period of performance from 31March2005 through 31August2006 which includes the no cost extension of FY2005 funded work. Year two (FY 2006 funds) were in place by 31May2006. However, there is no overlap of reported work.

Researchers at the University of Memphis completed year one effort by 31March2006 as reported in prior quarterly reports. Vanderbilt University is just now starting the year two funded efforts and the University of Alabama- Huntsville is not participating in year two. Consequently, all of the work reported in this Final Report was funded solely by the FY2005 funds. Therefore this report covers effort toward the Year One Annual Program Plan. The efforts under FY2006 funding from 31May2006 through 31August2006 are reported in a separately submitted first quarter report for FY2006 funds and are referred to as Year Two activities. All of this was discussed with Steven Murrill from the Army Research Laboratory (ARL), Adelphi, MD, our Cooperative Agreement Manager, to get his agreement to this reporting process.

1.2 Center Activities

The Director met frequently with Steven Murrill, to discuss year 1 activities and plans for year 2. Year Two plans called for increasing the number of supported researchers at The University of Memphis to five and eliminating the subcontract with the University of Alabama Huntsville.

1.2.1 Providing Support to Research Efforts

Center personnel provided continued support to research efforts at the Army Research Laboratory in the areas of sensor networks and Intelligence/Surveillance/Reconnaissance (ISR) sensors. This activity will continue as part of Year Two efforts.

The Army's Night Vision and Electronic Sensors Directorate (NVESD) was supported by frequent contact with Dr. Halford. Support was primarily for the Modeling and Simulation Division's research activities.

Dr. Halford continued to support Dr. Tim Edwards (under separated funding) from the Army's Redstone Technical Test Center (RTTC). Human perception measurements at the Center were obtained and reported. Interpretation of the data obtained in the perception experiments is still being analyzed.

1.2.2 Perception Laboratory

The Center's Perception Laboratory continues to support military research. The NVESD perception experiments in February, May and August were conducted at The University of Memphis. Additional experiments are planned for November, 2006. The laboratory will continually evolve but a complete set of the initially planned equipment is in place.

The sections that follow present a summary of first year activity on each of the milestones in the Annual Program Plan.

1.3 Milestone One: Build an ontology-based, knowledge repository of representative sensors

1.3.1 Purpose of Project Milestone

A high priority of the U. S. Military, and in particular the U.S. Army, is the requirement to integrate information from a variety of heterogeneous sensors and other information sources. The ability to discover a set of sensors based on a user's high-level query specification and to subsequently configure and receive data from these sensors for missions that may not have been anticipated at the time the sensors were deployed is critical. Ideally, such information integration will facilitate the construction of accurate situation assessment synthesized from shared data. Specifically, according to [Scherl, 2004] the Army's Future Force will carry out Network Centric Warfare, which is defined by [Alberts, 2002] as "an information superiority-enabled concept of operations that generates increased combat power by networking sensors, decision makers, and shooters to achieve shared awareness, increased speed of command, a higher tempo of operations, greater lethality, increased survivability, and a degree of self-synchronization." Therefore, the motivation of this project milestone was to investigate techniques by which sensors and sensor repositories could be described in a computer-readable format, that is, the development of an ontology-based knowledge repository of sensors. Such a knowledge base could be used to enable applications to locate, access, and in some cases, facilitate on-the-fly tasking of sensors in an automated manner via computer agents.

1.3.2 Background: Ontological Engineering

Since the 1980s, Ontological Engineering has been a subject of computing research, particularly in knowledge representation and automated reasoning. The work in ontologies centers on developing shared, machine readable conceptualizations of knowledge that can be used by intelligent computer systems. Representative work concerning ontologies includes [Lenat, 1989; Skuce, 1990; Uschold, 1996; Chandrasekaran, 1999] and more recent work in the context of the Semantic Web includes [Fensel, 2003; McGuinness, 2003]. The Semantic Web effort [Berners-Lee, 2001) focuses on defining and moving ontologies and knowledge representation standards from traditional, stand-alone systems, to the highly-distributed World Wide Web (WWW). Since networked sensors were our focus, the evolving infrastructure being standardized for the Semantic Web was viewed as the appropriate means for developing our sensor ontology and laboratory prototype environment. Much work in classical Artificial Intelligence research is seeing renewed application in the context of the Semantic Web [Russomanno, 2003].

As stated by [Llinas, 2004]: "One main benefit typically cited for basing the development of an information process on an ontological footing is: interoperability, with other local and also external processes, which leads to a shared understanding." Therefore, our year

one investigation has focused in part on the following: i) how an ontology of sensors can be defined and used to enable processes that require sensor interoperability and fusion; and ii) the development of a prototype environment for proof-of-concept use of the ontology.

1.3.3 Accomplishments

As part of CAS knowledge engineering year 1 activity, we have conducted a thorough literature survey related to sensor ontologies and approaches to sensor service specifications. We have implemented a computer-readable ontology and accompanying prototype environment. We have outlined an approach for locating sensors by semantic processing of an agent's query. Details of these accomplishments are described in the following paragraphs.

Computer-Readable Ontology

We developed a computer-readable sensor ontology and have coined it as OntoSensor [Russomanno, 2005]. This work deviated somewhat from the plans stated in the initial project proposal to focus primarily on defining imaging sensors in the ontology. This change in direction was, in part, because of the relative simplicity of the sensor nodes that were readily available from commercial vendors such as Crossbow, Inc. [Crossbow, 2006] as compared to the limited availability of complex imaging sensors. As such, the knowledge engineering activity focused on creating ontological information for low-cost wireless sensor network configurations to gain familiarity with sensor knowledge modeling techniques and available tools, before moving on to ontological modeling of complex imaging sensors. These simpler wireless sensors typically provide scalar samples rather than high-bitrate data sources such as video sensors or infrared (IR) cameras. In addition, capturing ontological information for these simpler sensors and motes enabled the rapid development of a prototype environment and facilitated graduate students to experiment with novel approaches for the design of software agents, sensor service brokers, and the utilization of Semantic Web infrastructure.

Graduate students K. Kothari, O. Thomas, and C. Goodwin (Kothari and Goodwin received partial support from CAS funds) made contributions to OntoSensor, including the instantiation of a variety of wireless sensor instances into the knowledge base. Our approach was that the specific sensor instances were to be specified in distributed repositories located at base stations throughout a network, while OntoSensor resided on a central server and contained categorical descriptions of the various sensors including their attributes and associations. A screen shot of OntoSensor is provided in Figure 1.1-1.

All sensors used in our prototype environment in laboratory Engineering Science (ES) 223 have associated computer-readable OntoSensor definitions. OntoSensor provides a basic knowledge base of various sensor types. The contents of OntoSensor can be exported to OWL [Smith, 2003] format and processed by any software with OWL

parsing capability. The export of OntoSensor is accessible via the following URL: <http://www.eece.memphis.edu/cas/OntoSensor/OntoSensor.owl>.

OntoSensor also includes knowledge models for a variety of data acquisition boards, sensing elements, and processor/radio units, as well as preliminary definitions for a few imaging sensors. OntoSensor concepts and associations are instantiated in distributed repositories updated by the base stations of the network. The data model for a given sensor provides containers for meta data such as sensitivity, performance range, and accuracy for the sensing elements, as well as physical characteristics such as mass, radio frequencies, dimensions, and power supply information for wireless motes.

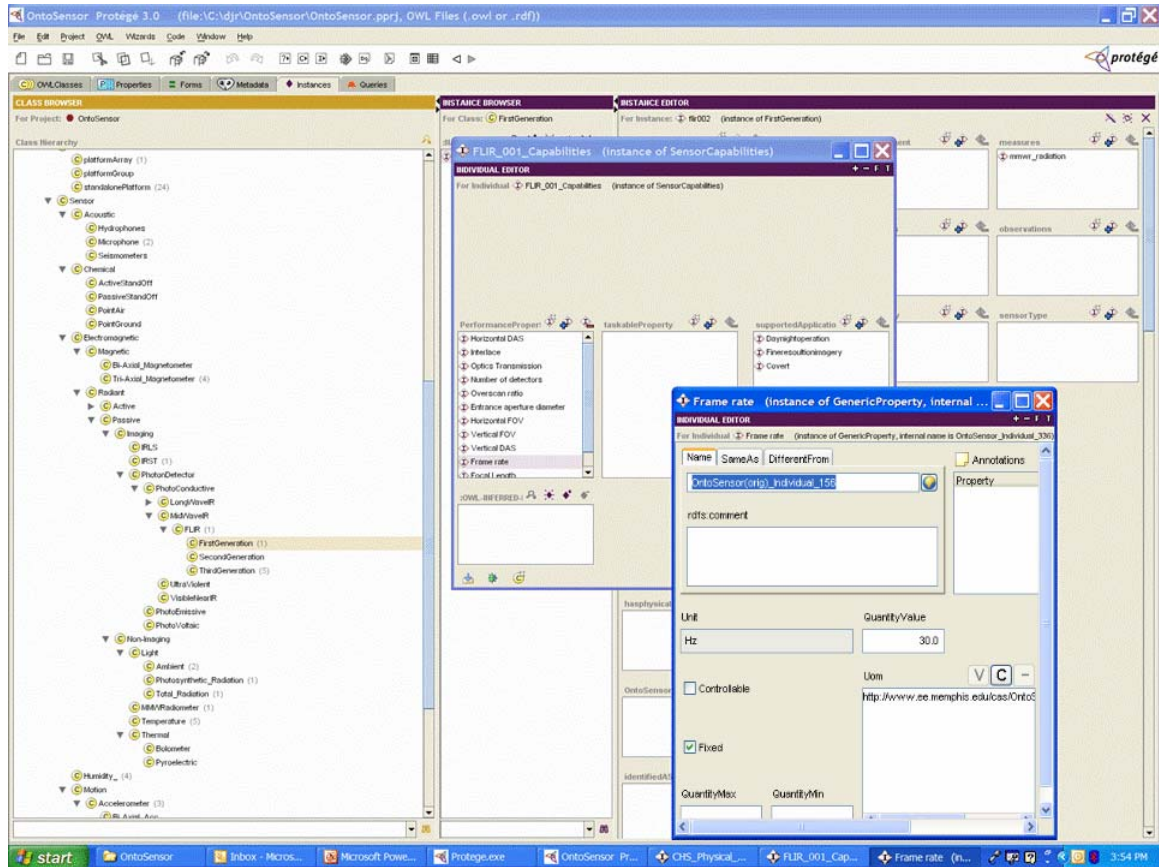


Figure 1.1-1: Screen shot of the OntoSensor interface using Protégé 2000

We also developed code for some basic queries of OntoSensor using SWI-Prolog libraries [Wielemaker, 2003] to illustrate a concrete approach of how the ontology could be accessed. The code is independent of the ontology but can read, parse, and perform inference on OntoSensor, which has been exported to OWL and posted to the Web.

Laboratory Prototype

The laboratory prototype implementation focused primarily on using ontological models of representative sensors commonly found in wireless network applications and the definition of an architecture for locating sensor services with capabilities and other properties that satisfy a user's query. This laboratory prototype effort included the

preparation/submission of a paper and poster to the *IEEE Fifth International Conference on Information Processing in Sensor Networks* [Goodwin, 2006]. This paper describes work-in-progress development of our ontology-based, sensor network prototype environment. The majority of the sensors, motes, and base stations used in the prototype were purchased from CAS funds.

The wireless environment consists of two networks, each having multiple sensor nodes built from parts available from commercial vendors as shown in Figure 1.1-2. Sensor types include models MEP410, MEP510, MTS420, and MTS310 available from Crossbow Inc. (examples are shown in Figure 1.1-3). The MEP410 and MEP510 are environmentally hardened mote platforms. The MEP410 platform sensing capabilities include ambient light, barometric pressure, photo-sensitive light, relative humidity, and temperature. The MEP510 platform is capable of relative humidity and temperature measurements. A MIB510 gateway is used for the aggregation of data obtained from the MEP410 and MEP510 platforms. Also, MTS420 and MTS310 data acquisition sensing elements are coupled with MICAz processor/radio boards. The MTS420 sensor boards have capabilities that include bi-axial accelerometer, ambient light, barometric pressure, temperature, GPS, photo-sensitive light, and relative humidity measurements. The MTS310 sensor boards have bi-axial accelerometer, bi-axial magnetometer, acoustic, temperature, and photo-sensitive light sensing elements. The MTS420 and MTS310 deployment uses a MIB520 network gateway which collects data from remote deployments. The MICAz boards operate in the 916 MHz or 2.4 GHz frequency range and handle the data processing and communication needs for the platform. The processor/radio boards run Crossbow's XMesh software that allows dynamic formation of communication links between the nodes.

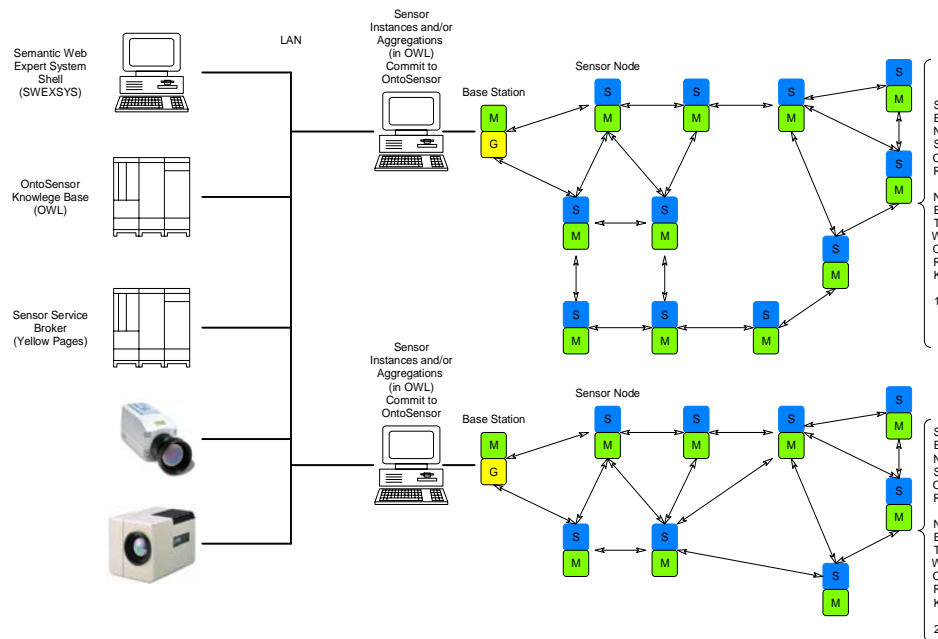


Figure 1.1-2: Prototype Sensor Network Constructed in Engineering Science (ES) 223



Figure 1.1-3: Example wireless sensor nodes and motes used in the development of the prototype environment.

Currently, two computers interface with the associated base stations using Crossbow's MoteView application to retrieve data which is stored in a PostGRE database. Each base station executes custom software developed by C. Goodwin that generates OntoSensor referenced OWL repositories from the collected sensor data. The software is a preliminary implementation of a web service that will be evoked at the base stations for exchanging OWL data within the network environment.

The software executing on each base station periodically checks for a database update using PostGRE ODBC drivers and retrieves updated tuples corresponding to raw sensor percepts. The retrieved tuples are then post-processed and marked up using OWL and made available for potential data sharing with other processes.

Additional laboratory activity included experimenting with the various Crossbow Inc. sensors and motes to gain an understanding of their sensing capabilities, programmable features and suitability for potential ontology-based proof-of-concept applications within the context of our prototype environment.

Literature Survey

We performed an extensive literature survey for related efforts. Our survey indicates that although OntoSensor is somewhat superficial in content, it is considerably more detailed, for a given sensor type, than other sensor ontologies that are freely available. For example, OntoSensor provides more details about the sensor types and instances defined in its knowledge base than the SWEET sensor ontology [Raskin, 2006] provided by the Jet Propulsion Lab accessible via the following URL: <http://sweet.jpl.nasa.gov/sweet>. SWEET may provide more sensor types than OntoSensor, but provides no computer-readable details about the various sensor types.

We also monitored and analyzed the Open Geospatial Consortium's evolving specification of SensorML. SensorML is part of the SensorWeb enablement effort which shares many of the same goals of our work in sensor interoperability, discovery, on-the-fly tasking, etc., but this effort does not currently employ Semantic Web infrastructure. Moreover, many of the class diagrams provided in the SensorML specification are

generic and, when used alone, lack the detail and semantics for creating a sensor ontology. However, the possibility of augmenting SensorML specifications with concepts from one or more formal ontologies may be a promising approach.

Our design of OntoSensor was based (in-part) upon a draft SensorML specification [OGC 04-019, 2004]. The 2004 SensorML specification has subsequently undergone substantial revisions [OGC 05-086r2, 2006]. Nevertheless, our initial approach to the implementation of OntoSensor is continuing to be used in our prototype environment. However, there is an opportunity and need to re-organize OntoSensor to better complement the revised SensorML specification, which may provide wider visibility, utility, and adaptation of our approach to sensor ontology realization.

Sensor Services

We investigated various approaches for defining and implementing sensor services for the prototype environment such that an agent can locate services based on a high-level query and subsequently receive data from and/or task the sensors. A service-oriented architecture [Singh, 2005], in which sensors publish their availability to a sensor service broker that provides a type of yellow-pages description of sensor services, can be queried by a sensor service requestor to locate sensors having certain properties that might satisfy both a geographic as well as capability constraints. A generic model for sensor services is shown in Figure 1.1-4. Sensors have corresponding service definitions (function declarations that are accessible over the network) that include binding information such that a requestor can query and/or task the sensor, sensor network, or base station. In our approach, the sensor service providers are the actual individual sensors, sensor networks or base stations that register their respective services with the broker and publish their associated OWL repositories on the network.

Both Sun Microsystems [Horan, 2005] and Microsoft [Liu, 2005a; Woo, 2005; Liu, 2005b] have basic research efforts related to this area. In addition, the Naval Research Laboratory (NRL) [Luo, 2005] defines an approach to support semantic service description and match making with registries that use the existing Universal Description, Discovery and Integration (UDDI) V3 specification.

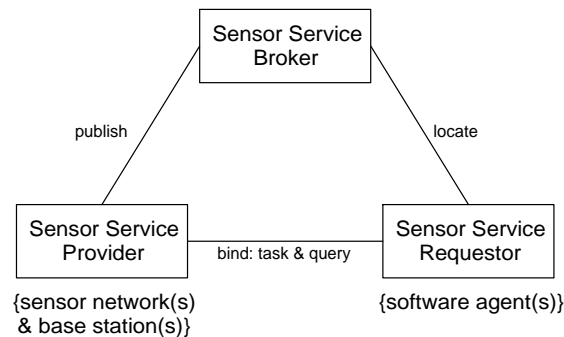


Figure 1.1-4: Generic Model for Sensor Services

Our activity focused on the matching process of finding the appropriate sensors for a given high-level query using knowledge-based support that is not part of the sensor

service broker's registry. Unlike the NRL approach taken by [Luo, 2005], which provides a method to bulk-load semantic data into UDDI TModels, our activity focused on developing an approach to associate OntoSensor with a UDDI registry of sensor services to support semantic searching. A simplification of our approach is shown in Figure 1.1-5. In this scheme, the UDDI database can be viewed as a sensor services cache. If the agent's query results in hits, that is, sensor services that match the user's request are directly specified in the UDDI registry, then, these sensors' bindings (specifications to query and/or task the sensor) are returned to the agent; otherwise, the UDDI sensor service interface will attempt to find generalizations or specializations via OntoSensor that may semantically match (to some degree) the agent's query. If such matches are found, then, they will be directly updated in the UDDI registry, much like a conventional cache, for rapid retrieval of subsequent solutions to agent's queries.

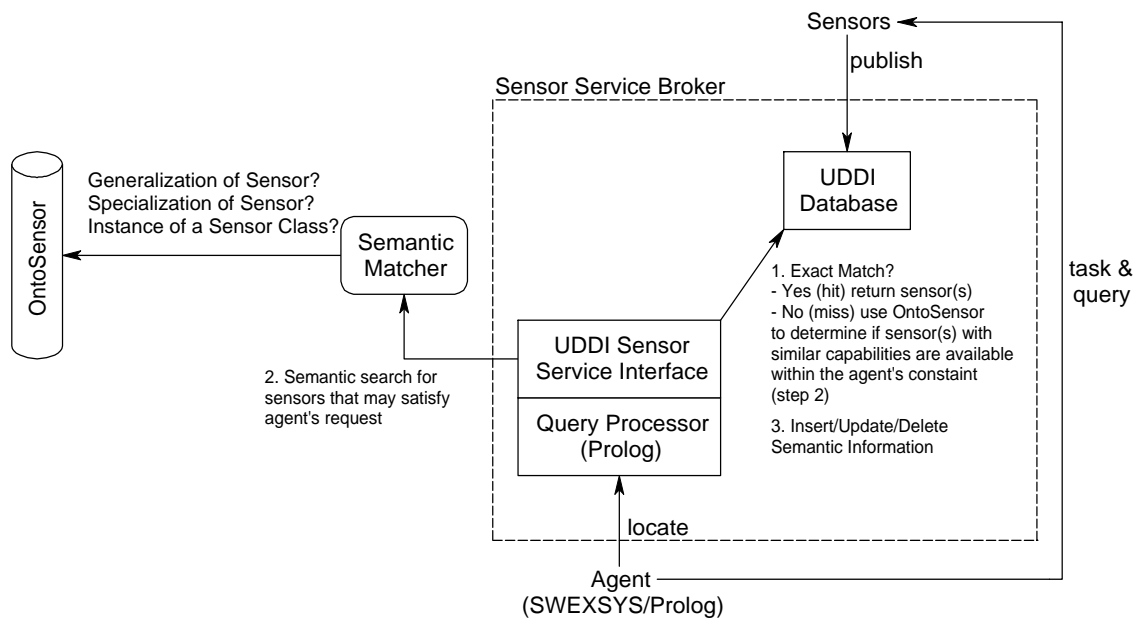


Figure 1.1-5: Sensor semantic service description and match approach for prototype

1.3.4 Future Work

OntoSensor and Prototype Enhancements

As previously reported, it is possible that OntoSensor may have the potential for wider adoptability, contributions, and assessment from a variety of user communities if it is reorganized to better complement the revised OGC SensorML specification. Knowledge reorganization of OntoSensor is needed in year 2, while continuing to use the current model in the prototype environment to support development of the sensor service and agent functionality.

To support a variety of possible tests and proof-of-concept applications, future prototype enhancements require the inclusion of more complex sensors into OntoSensor and the network including imaging sensors such as video, visible, infrared, terahertz and other sensors that provide rich, high-bitrate data. For example, a ThermoCam Merlin mid-wave infrared camera (or similar camera) and other CCD cameras are currently pending integration into the prototype environment. Cameras such as Merlin connect directly to the LAN and include a software development toolkit (SDK). Ideally, we would use the SDK to develop service descriptions such that the cameras could be queried and tasked by agents that locate the cameras' services via the broker without requiring detailed knowledge of the sensors' device drivers or API.

The SDK will also be used for obtaining periodic frames and marking up knowledge about captured images in OWL. These images and their associated OWL repositories will be stored at the associated base stations that can be subsequently discovered and queried by agents and end users. The OWL repositories will contain meta data that includes image format, date, time, resolution, location and other properties about the sensor that captured the images and the surrounding environment. The meta data contained in OntoSensor describing cameras may be used to deduce further information about their acquired image. Furthermore, a time series of images can be retrieved from a distributed repository and post-processed to extract intrinsic knowledge that can be combined with scalar-level readings such as temperature, vibration, acoustic, magnetic field measurements, or other information sources to potentially increase the confidence in a target or activity of interest.

Additional work is needed to further implement the sensor service architecture outlined in Figure 1.1-5. Currently, the agent is only capable of examining a simple database of URLs to locate and load sensor repositories from the various base stations into its knowledge base to perform simple queries and reasoning processes. The ability for the agent to perform semantic searching and selection and the capability to combine web services using the scheme outlined in Figure 1.1-5 is desired.

OntoSensor may be further extended using open standards provided by OWL-S [Martin, 2004] to capture higher-level knowledge about sensor services. From the view of the sensor service requestor (agent), the deployed networks will appear as a seamless environment that provides a set of services. Realization of this environment will require implementation of a comprehensive sensor service broker.

References

[Alberts, 2002] D. Alberts, J. Garstka and F. Stein, *Network Centric Warfare: Developing and Leveraging Information Superiority*, CCRP, 2002.

[Berners-Lee, 2001] T. Berners-Lee, J. Hendler and O. Lassila "The Semantic Web: A new form of Web Content that is meaningful to Computers will unleash a revolution of new possibilities," *Scientific American*, May, pp. 34-43, 2001.

- [Chandrasekaran, 1999] B. Chandrasekaran, J. Josephson and V. Benjamins "What are ontologies and why do we need them?" *IEEE Intelligent Systems*, 14(1), pp. 20-26, 1999.
- [CrossBow, 2006] CrossBow Technology Inc., *Wireless Sensor Networks: Product Reference Guide*, 2006.
- [Fensel, 2003] D. Fensel, F. van Harmelen, and I. Horrocks "OIL and DAML+OIL: Ontology Languages for the Semantic Web," In *Towards the Semantic Web: Ontology-Driven Knowledge Management* (J. Davies, D. Fensel, and F van Harmelen, eds.), pp. 11-31, West Sussex, England: John Wiley and Sons, Ltd., 2003.
- [Goodwin, 2006] C. Goodwin and D.J. Russomanno, "[An Ontology-Based Sensor Network Prototype Environment](#)," *Fifth International Conference on Information Processing in Sensor Networks (Poster)*, IEEE, Nashville, TN, pp. 1-2, 2006.
- [Horan, 2005] B. Horan, "[The Use of Capability Descriptions in a Wireless Transducer Network](#)," *SML Technical Report Series: SMLI TR-2005-131*, Sun Microsystems Laboratories, pp. 1-3, 2005.
- [Lenat, 1989] D. Lenat and R.V. Guha (1989) *Building Large Knowledge-Based Systems: Representation and Inference in the CYC Project*, Reading, MA: Addison-Wesley, 1989.
- [Liu, 2005a] J. Liu and F. Zhao, "[Towards Semantic Services for Sensor-Rich Information Systems](#)," *Second IEEE/CreateNet International Workshop on Broadband Advanced Sensor Networks*, Boston, MA, Oct. 3, 2005.
- [Liu, 2005b] J. Liu, E. Cheong, and F. Zhao, "[Semantics-Based Optimization Across Uncoordinated Tasks in Networked Embedded Systems](#)," *Proceedings of the 5th ACM Conference on Embedded Software (EMSOFT 2005)*, Jersey City, New Jersey, September 18-22, 2005.
- [Llinas, 2004] J. Llinas, C. Bowman, G. Rogova, A. Steinberg, E. Waltz and F. White (2004) "Revisiting the JDL Data Fusion Model II," *The 7th International Conference on Information Fusion*, Stockholm, Sweden, pp. 1218-1230, 2004.
- [Luo, 2005] J. Luo, B. Montrose, and M. Kang "[Adding Semantic Support to Existing UDDI Infrastructure](#)," *Report No. NRL/MR/5540--05-8918*, Naval Research Laboratory, Code 5542, 2005.
- [Martin, 2004] D. Martin, M. Burstein, J. Hobbs, O. Lassila, D. McDermott, S. McIlraith, S. Narayanan, P. Paolucci, B. Parsia, T. Payne, E. Sirin, N. Srinivasan and K. Sycara, "OWL-S Semantic Markup for Web Services," W3C submission, 2004.
- [McGuinness, 2003] D. McGuinness "Ontologies Come of Age," In *Spinning the Semantic Web* (D. Fensel, J. Hendler, H. Lieberman and W. Wahlster, eds), pp. 171-195, Cambridge, MA: The MIT Press, 2003.

[OGC 04-019, 2004] M. Botts (editor) "Sensor Model Language (SensorML) for In-situ and Remote Sensors," *OGC 04-019*, Open Geospatial Consortium Inc., 2004.

[OGC 05-086r2, 2006] M. Botts (editor) "[Sensor Model Language \(SensorML\) for In-situ and Remote Sensors](#)," *OGC 05-086r2*, Open Geospatial Consortium Inc., 2006.

[Raskin, 2006] R. Raskin, "Guide to SWEET Ontologies," NASA Jet Propulsion Lab, <http://sweet.jpl.nasa.gov/guide.doc>, 2006.

[Russomanno, 2005] D.J. Russomanno, C. Kothari, C., and O. Thomas, "[Building a Sensor Ontology: A Practical Approach Leveraging ISO and OGC Models](#)," *Proceedings of the International Conference on Artificial Intelligence (ICAI 2005)*, Las Vegas, NV, 2005.

[Russomanno, 2003] D.J. Russomanno and C. Kothari "An Implementation of Plausible Inference for the Semantic Web," *The International Conference on Information and Knowledge Engineering (IKE03)*, Las Vegas, Nevada, pp. 246-251, 2003.

[Sherl, 2004] R. Scherl and D. Ulery (2004) "[Technologies for Army Knowledge Fusion](#)," *Technical Report ARL-TR-3279*, 2004.

[Singh, 2005] Singh, M., and Huhns, M. *Service-Oriented Computing*, West Sussex, UK: John Wiley & Sons, 2005.

[Skuce, 1990] D. Skuce and I. Monarch "Ontological Issues in Knowledge Base Design: Some Problems and Suggestions," *CMU-CMT-90-119*, Pittsburgh, PA: Carnegie Mellon U., 1990.

[Smith, 2003] M. Smith, et al., OWL Web Ontology Language Guide: W3C Proposed Recommendation. Online Resource: <http://www.w3.org/TR/2003/PR-owl-guide-20031215/>, 2003.

[Uschold, 1996] M. Uschold and M. Gruninger "Ontologies: Principles, Methods, and Applications," *Knowledge Engineering Review*, 11(2), pp. 93-115, 1996.

[Wielemaker, 2003] Wielemaker, J., Schreiber G., and Wielinga, B., "Prolog-based Infrastructure for RDF: Scalability and Performance," In *Proceedings of the 2nd International Semantic Web Conference*, Sanibel Island, FL, 2003, pp. 644–658, 2003.

[Woo, 2005] A. Woo, S. Seth, T. Olson, J. Liu, and F. Zhao, "[A Spreadsheet Approach to Programming and Managing Sensor Networks](#)," *Technical Report MSR-TR-2005-162*, Microsoft Research, Redmond, WA 98052, November 2005.

1.4 Performance modeling of sensors with image processing enhancements

The use of image processing enhancements in sensors is now widely accepted. The techniques include ATRs, image fusion, local area processing (such as local contrast enhancement), image stabilization, super resolution (primarily reconstruction with undersampled imagers) and turbulence mitigation. Other techniques such as boost and logarithmic amplification can also be considered although they are not necessarily done by processing the imagery. Color presents another opportunity for image processing enhancement. Color can be coupled with image fusion to present the fused image in an optimum manner.

1.4.1 Milestone: Establish methodology for incorporating image processing techniques into existing performance models.

Each of the techniques has been studied to determine an effective means of incorporating their effects into a sensor model. The status of this milestone is summarized by considering each technique.

Image stabilization in effect reduces the blur. Its incorporation into a sensor model is therefore accomplished by determining the equivalent reduction in motion of the imager. Blur due to motion is well understood so the effect of its reduction is readily incorporated into a sensor model.

Local contrast enhancement can also be readily incorporated into sensor models. The local area contrast rather than scene contrast is used to determine human performance.

Turbulence mitigation can similarly be incorporated by determining an effective value of C_n^2 , the structure constant for the index of refraction. Much work remains for this technique, but its incorporation into the sensor model is now clear.

Super resolution is treated in a similar manner, except that the technique affects two sensor parameters. The performance improvement is mapped into a resolution/noise space. For example, the process is known to decrease noise and increase resolution. This provides a means of quantitatively expressing the improvement afforded by the processing. Both of these parameters impact human discrimination in well studied manners. Consequently, super resolution algorithms are readily modeled as changes in resolution and noise. While this was reported in the first quarter report it is repeated here because it has been used and seems to provide satisfactory results.

Modeling ATRs remains an active area of work within the Center. Specifically, the anomaly detection algorithm reported by Singer is the ATR being modeled [Singer, 1999]. However, our work has identified two means of incorporating the ATR performance into the sensor model. They differ in their methods of obtaining the signal-to-clutter (SCR) ratio. One technique requires an image whereas the second uses

previously determined parameters from typical imagery to characterize the power spectral density of the background. It also requires spectral properties of representative materials such as paints, grass, asphalt, bricks and cinder block. This model represents an original contribution that will form the basis of a journal submission. It is considered the best way to incorporate ATR models into a sensor mode. This is because most sensor models are physics-based models and do not utilize imagery as an input. More detail is provided in Sections 1.4.2. The emphasis of the model is for infrared imagers, primarily those operating in the mid wave and long wave IR.

The SCR can be considered a generalization of the signal to noise ratio (SNR), often used to quantify the performance of a single band imaging system. The SNR is simply the magnitude of the target divided by the standard deviation of the background. SCR generalizes SNR to handle multiple spectral bands and spatial processing.

Once the SCR is estimated, receiver operating characteristic (ROC) curves can be obtained for some algorithms. For the Singer algorithm [Singer, 1999], the SCR determines the non-centrality parameter for the non-central F distribution. Basically, the cumulative distribution function of the non-central F distribution is the ROC curve for the ATR. As always, such a result depends on modeling assumptions. For example, an assumption of Gaussian statistics for pixel distribution leads to the non-central F distribution. It is apparent that Gaussian statistics may not represent the tails of the distribution well. And, the tails of the distribution are the critical pixels for a detection process where atypical pixels are being sought. However, such assumptions are likely to have little impact on comparative uses of the model, one sensor vs. another, one band vs. two, different spectral bands (band selections). Furthermore, the SCR is likely the critical parameter for almost any ATR algorithm, even if the ATR algorithm does not lend itself to analytical modeling.

1.4.2 Milestone: Determine sensor performance enhancement offered by anomaly detection ATRs.

1.4.2.1 Algorithm Description for SCR Calculation

The steps of the algorithm for estimating a SCR for a sensor are enumerated below. They indicate some of the information required as well as what sensor aspects are treated. Most of the input parameters come from models obtained from measured data. The actual ATR algorithm is run to calculate the final SCR. This provides a means to perhaps generalize the model to many different algorithms. That generalization was not developed. The Singer algorithm [Singer, 1999] was chosen as representative of the performance that could be obtained with an anomaly detection algorithm.

The model calculations are performed in several separate steps to generate the required input data and calculate intermediate results. These divisions are:

1. Optics calculations
2. Background spatial shape

3. Background spatial autocorrelation
4. Target spatial shape
5. Sensor spectral responses to target and background
6. Spectral covariance
7. Noise
8. Target vector
9. Background vectors (forms a matrix)
10. Clutter covariance matrix
11. Target and background response vectors and noise response
12. Spectral anomaly detector matrix
13. Output SCR

Each of these steps forms a block of the overall ATR (SCR) model.

The SCR is a measurement of the amount of independent information about a target obtained from a sensor in both the spectral and spatial domains. Adding additional spectral bands increases the amount of raw data collected, but the amount of useful information only increases if the new bands return some uncorrelated data. Similarly, spatial filtering will give more information about the locations of possible targets only when the target shape and the clutter shapes are different.

The SCR measures the relative amount of information available upon which to perform target detection with a space-spectral anomaly detector style ATR. Increasing the amount of input information is assumed to increase the final performance of a general ATR algorithm. This model does not model any specific ATR implementation or any additional processing such as target trackers.

1.4.2.2 Spectral Radiance Model

The model requires a spectral model of the target and background. One such model is presented. It uses planar surfaces in the form of a box sitting on a plane and located near a planar wall. The box is a tank-sized box and the wall can represent a building or a tree line, depending on what materials are specified. This model is intended to give quick and useful spectral target radiance predictions without a high level of expertise in thermal prediction being required by the user. This model is an effective tool for comparisons of different sensors or for band selection.

To simplify the calculation of spectral radiance, some assumptions have been made about the materials and surfaces. All materials and surfaces are assumed to be opaque and Lambertian. The opaque assumption avoids the need to handle translucent materials. Assuming opaque materials allows the material properties to be fully specified by either reflectance or emittance. Very few materials are translucent in the infrared bands. The Lambertian assumption allows geometric calculations to be separated from spectral calculations. This greatly reduces the amount of calculation necessary. Most materials are close to Lambertian in the infrared. Handling non-Lambertian surfaces would greatly complicate the model.

A single target and background geometry with 4 look angles has been chosen to simplify the spectral radiance model. The target, wall, and ground and the 4 view angles are shown in Figure 1.4.2-1. The assumed target consists of a roughly tank-size box 6m long, 3m wide, and 2m high. It is located 10m away from a 12m high wall of essentially infinite length. The 4 views are 0° , 0.1 radian declination, 45° declination, and 90° declination. The 0° and 0.1 radian views are typical of ground-to-ground engagements. The 45° view is intended to model an Unmanned Aerial Vehicle (UAV) view. The 90° view models UAV, aircraft, or satellite views.

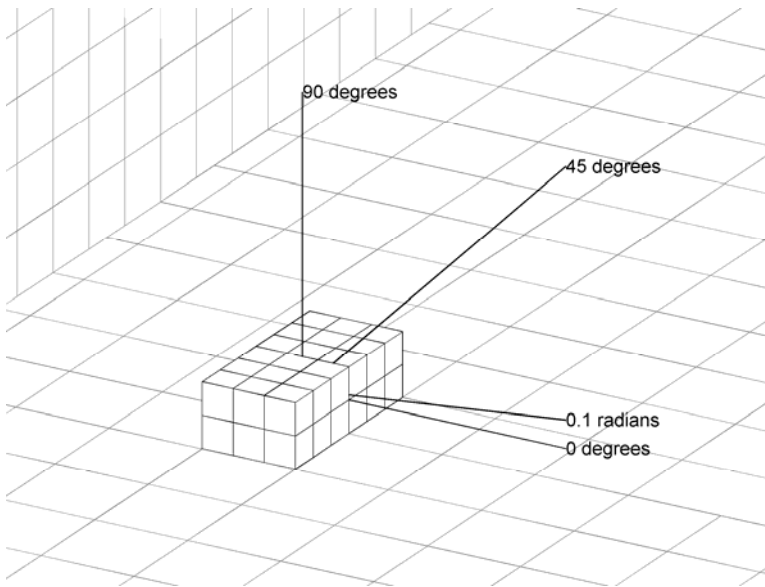


Figure 1.4.2-1: box and wall geometry

The radiometric parameters for this modeled have been worked out through numerical integrations, validated by limiting cases for which analytical solutions exist. MODTRAN can be used in conjunction with this model to obtain the effects of sky radiance and solar illumination. With the spectral characteristics of the materials, one can obtain the radiance for the sensor with any of the chosen orientations.

1.4.2.3 Model Validation

Numerical validation is difficult to obtain. Instead, the model is validated for trends and tendencies. The model predicts that for certain choices of materials and bands, two bands provide a higher SCR than a single band. Similarly, three bands (properly chosen for materials assumed) provides a higher SCR than two bands. The same prediction is available from analysis of actual imagery and from actual ATR algorithms.

It is not a general truth that two bands are always better than one or that three bands are always better than two. This two is borne out in the model predictions.

The details of the model are being prepared for submission to a suitable journal for publication.

1.4.3 Milestone : Modify/adapt existing sensor models to account for the improvements offered by image fusion.

This activity is still in process and expected to remain an active area into year two of this grant. Progress has been made in establishing a process. However, the process involves extensive perception laboratory testing to quantify the improvement. The use of color has generated considerable interest. Consequently, color models were studied and significant results are the subject of a paper being submitted for publication [Krapels, 2007].

The details of the fusion work accomplished to date are provided. Perception experiments are scheduled for August, 2006 to provide some validation/calibration of the metrics. More imager may become available leading to additional perception experiments if warranted. Otherwise, this effort may be concluded by the mid point of the second year of Center activities.

1.4.3.1 Fusion Introduction

Several fusion algorithms are discussed. The described fusion methods are applied to LWIR and MWIR images of urban scenes. Several image fusion metrics are described as well and applied to analyze images fused using the reviewed techniques. The results of a paired comparison perception test are then analyzed to see in what order the images are preferred by observers. The observer preference is then compared with the fusion metrics to see which metric best correlates to the observer preference.

Despite the very active research in computer vision, many image related tasks are best performed by human observers. It is also noted that images from different spectral bands can often provide complimentary information. In order to fill the human visual information channel, there is a need to fuse images from different imagers. The hope is that successfully fused imagery will provide to the observer with the important information from all of the source images while causing the least possible amount of distortion, noise, or image quality degradation. For fusion to be worth while, fused images must allow for better observer performance than either of the source images.

There are many issues that must be addressed for successful image fusion to take place. First, the images to be fused must be registered. The imagers should have similar fields of view and detector resolution. The images also should be obtained sufficiently close to one another both spatially and temporally. If these conditions are not met, fusion may not be possible. Different tasks may also dictate how much time and computing power is available for fusion to take place. Another issue is whether or not fused issues should be displayed as monochromatic or color images. Toet [Toet, 2003] has shown that appropriate color maps can be beneficial for task performance using fused imagery and

better fill the visual channel. He also observed that inappropriate color maps actually cause observer performance to drop below that possible with monochromatic images. In this report we will report results from a perception experiment using grayscale fused imagery. Another issue is that noise can be introduced in the fused image through either of the source images or by the fusion technique itself. Since the visual channel is bandlimited, image fusion often requires that some information in the source images be attenuated or eliminated. The different fusion algorithms reviewed here show different attempts to select and combine the relevant information from source images into a single fused image.

1.4.3.2 Fusion Techniques

Pixel by pixel averaging is the most common of the image fusion techniques. It is simple and can be implemented in real-time with both analog and digital systems. Averaging does not perform well when images to be fused have areas of opposing contrast. This destructive interference can result in a fused image with decreased contrast for important features visible in both of the image bands.

Gabor image fusion uses a concept from psychophysical data which suggests that human observers weight the visual information they receive based on spatial frequency and orientation. In the spatial domain the Gabor functions can be represented in this form:

$$g(x, y) = K \exp\left(-\pi\left(a(x - x_0)^2 + b(y - y_0)^2\right)\right) \exp(j(2\pi(u_0 x + v_0 y) + P)) \quad (1.4.3.1)$$

In the equation above, K determines the magnitude of the envelope. The terms a and b scale the axes of the Gaussian envelope. x_0 and y_0 give the location of greatest intensity in the Gaussian envelope. P represents the phase of the sinusoid. Together u_0 and v_0 determine the frequency of the sinusoid. In the frequency domain the Gabor functions can be represented as filters that are the products of wedges and annuli.

In Gabor fusion, each of the source images is passed through a bank of Gabor filters that divide the image into bands depending on spatial frequency and orientation. For a given Gabor filter band, the magnitude of the transform of each image is compared. The image with the greatest magnitude in the band is then used in the construction of the fused image. In this way the most important parts of each source image are combined to produce the fused image.

The Discrete Wavelet Transform image fusion method is another technique that involves dividing the source images into frequency bands and then constructing a fused image using source image bands with the highest magnitudes. The difference between the DWT and Gabor techniques lies in the way that the images are divided into bands. The DWT is given below:

$$\begin{aligned}
W_{\psi}^i(j, m, n) &= \frac{1}{\sqrt{MN}} \sum_{x=1}^{M-1} \sum_{y=1}^{N-1} f(x, y) \psi_{j,m,n}^i(x, y) \\
W_{\varphi}(j_0, m, n) &= \frac{1}{\sqrt{MN}} \sum_{x=1}^{M-1} \sum_{y=1}^{N-1} f(x, y) \varphi_{j_0,m,n}(x, y)
\end{aligned} \tag{1.4.3.2}$$

In the above equations, ψ is the wavelet basis function, and φ is the scaling basis function. W_{ψ} and W_{φ} are the wavelet and scaling approximations of the image.

The Shift-Invariant Discrete Wavelet Transform fusion technique addresses the fact that the DWT is not shift invariant due to the downsampling that it uses in its filtering process. This can cause visible artifacts in DWT fused images that are not perfectly registered. To overcome this problem, the DWT was made shift-invariant by omitting the downsampling process. This gives shift-invariances, but it is at the expense of computing efficiency.

In Principal Component Analysis fusion, images to be fused are expressed as column vectors of their pixels values. The two columns that results become the two columns of X . The PCA transform is defined as

$$Y = A(X - m_x) \tag{1.4.3.3}$$

Here X contains the source images, m_x is the mean of X , A is the matrix of eigenvectors of X , and Y is the transformed data. The fused image Y of the zero-mean image is then added to the pixel average of the two source images. Here $F(x, y)$ is the fused image, $F_d(x, y)$ is the output of the PCA transform, and $F_{avg}(x, y)$ is the average of the two source images.

$$F(x, y) = \alpha F_{avg}(x, y) + \beta F_d(x, y) \tag{1.4.3.4}$$

Each of the image fusion techniques discussed above (with the exception of Gabor fusion), were applied to LWIR and MWIR images of an urban scene. The original and fused images are shown below:



Figure 1.4.3-1 MWIR image

LWIR image



Figure 1.4.3-2 Pixel-averaged image

DWT image



Figure 1.4.3-3 PCA image

SIDWT image

1.4.3.3 Image Fusion Metrics

Mutual Information uses the entropy of an image to approximate the amount of information in a fused image. For a fused image f that results from two input images a and b , the mutual information is defined as

$$I(a, b, f) = H(a, b) + H(a - b) - H(a, b, f) \quad (1.4.3.5)$$

Where entropy is defined as:

$$H(X) = -\sum_i P_X(x_i) \log_2(P_X(x_i)) \quad (1.4.3.6)$$

The first two entropy terms describe the input images and increase the mutual information value. The third term considers information present in the fused image that

was not present in the source images to be noise. For this reason the third entropy decreases the resulting value of the mutual information.

The other fusion metrics used here (fusion quality index, weighted fusion quality index, edge-dependent fusion quality index) are based on the image quality index. The definition of the image quality index is given below:

$$Q_0 = \frac{4\sigma_{xy}\overline{xy}}{(\overline{x}^2 + \overline{y}^2)(\sigma_x^2 + \sigma_y^2)} = \frac{\sigma_{xy}}{\sigma_x\sigma_y} \cdot \frac{2\overline{xy}}{\overline{x}^2 + \overline{y}^2} \cdot \frac{2\sigma_x\sigma_y}{\sigma_x^2 + \sigma_y^2} \quad (1.4.3.7)$$

Q_0 are found for a moving window and then averaged together to give the quality of an image relative to another image. The resulting Q_0 term is a value between -1 and 1.

The fusion quality index compares a fused image to its two source images and produces an output between -1 and 1. It is determined from the Q_0 terms and the relative weights, $\lambda(w)$, of the input images. $\lambda(w)$ is a number between 0 and 1 that describes the relative weighting of a source image in the fused image. The weight is determined by the ratio of an image's saliency to the sum of the saliencies of both of the images. We used the variance to represent the salience of windowed sub-image. Fusion quality index is defined as

$$Q(a, b, f) = \frac{1}{|W|} \sum_{w \in W} (\lambda(w)Q_0(a, f | w) + (1 - \lambda(w))Q_0(b, f | w)) \quad (1.4.3.8)$$

The weighted fusion quality index weights individual windows in the image according to the total saliency of the image in that window. This is different from the fusion quality index, which weights all windows in an image equally. A window's saliency is given by

$$C(w) = \max(s(a | w), s(b | w)) \quad (1.4.3.9)$$

The calculation of the weighted fusion quality index varies only slightly from that of the fusion quality index

$$Q(a, b, f) = \frac{1}{\sum_{w' \in W'} C(W')} \sum_{w \in W} C(W) (\lambda(w)Q_0(a, f | w) + (1 - \lambda(w))Q_0(b, f | w)) \quad (1.4.3.10)$$

The intention of the weighted fusion quality index is to give more weight to areas of the image where more information is present. If the variance is a good indicator information content, this metric should yield more meaningful results than the fusion unweighted fusion quality index.

The edge-dependent fusion quality index is an extension of the weighted fusion quality index. It is the weighted fusion quality index of the two input images multiplied by the weighted fusion quality index of the two extracted edge images. This is done to model

the importance edges in images to human observers. The edges are extracted from the input images by convolution with a high pass filter kernel. The equation for the edge-dependent fusion quality index is given below in terms of the weighted fusion quality indices.

$$Q_E(a,b,f) = Q_w(a,b,f)Q_w(a',b',f'') \quad (1.4.3.11)$$

In the Mannos-Sakrison filter technique the fourier transform of the input and fused images are multiplied by a bandpass filter that describes the sensitivity of the human eye to spatial frequencies. The filter expressed in the frequency domain is

$$\Theta(r) = 2.6(0.0192 + 0.144r)e^{-(0.144r)^{1.1}} \quad (1.4.3.12)$$

In the equation above r is equal to the radius in pixels from the center of the shifted two dimensional fourier transform. The mean squared error of the filtered fused image to the each filtered input image is found.

Using the different fusion metrics discussed here, the fused LWIR/MWIR images from the urban scene shown previously were measured. The results are shown in the following table:

	FQI	WFQI	EDFQI	MINF	MS(F-L)	MS(F-M)
Average	0.7783	0.8433	0.5810	4.6896	3257.8	7037
DWT	0.7263	0.8916	0.7468	3.2733	1218.9	206.9
PCA	0.6011	0.8710	0.6842	3.5897	1067.9	173.9
SIDWT	0.7854	0.8723	0.6870	3.8848	656.3	218.5

Table 1.4.3-1 Summarizes the results of the different metrics for fused imagery.

1.4.3.4 Perception Test to Determine Observer Preference

The results from the different fusion metrics are clearly mixed. Different measures of image fusion give different preference orders. A paired comparison perception test was performed using a group of human observers [Silverstein, 2001]. Two pairs of registered LWIR and MWIR images were used as the source images. For a given scene, each observer was shown pairs of images fused using PCA, pixel averaging, Gabor wavelets, discrete wavelet transform, and the shift-invariant discrete wavelet transform. The original LWIR and MWIR images were also used in the comparison test. The observer indicated for each image pair which image was of better quality. For each observer a preference matrix was constructed from the test results. In the matrix, term C_{ij} represents the number of times that an observer preferred image i over image j . The individual preference matrices are all summed together for analysis. The preference matrix can be used to find the percent of the trials in which one image is preferred over another. The difference in perceived quality between the two images, $q_i - q_j$, can then be measured between the two images in the following way:

$$d'_{ij} = q_i - q_j \approx \sqrt{2}Z\left(\frac{C_{ij}}{C_{ij} + C_{ji}}\right) \quad (1.4.3.13)$$

In the above equation Z is the inverse cumulative-normal function. Here the assumption is made that observer preference increases along a cumulative normal as the image quality increases. So, from a matrix of C_{ij} values a matrix of d'_{ij} terms can be constructed. Knowing the distances in quality between each pair of images, all the images can be plotted along a one dimensional line after one of the images is arbitrarily assigned a q value as a reference. A problem occurs if there exists a pair of images in which one image is always preferred over the other across all of the observers. In this case, the Z function returns infinite values and a difference in quality cannot be estimated.

For this method of analysis the following assumptions must be valid:

1. Each sample must have a single value that can describe its quality q_i .
2. Each observer estimates the quality of this sample with a value from a normal distribution around this actual quantity.
3. Each sample has the same perceptual variance.
4. Each comparison is independent.

The results of this test will tell which fusion method observers feel provides them with the greatest amount of information with the minimum distortion. The quality values found in the perception experiment will be correlated with the results of the fusion metrics described previously. The metric which best fits the output of the paired comparison test is likely to be the most useful measurement tool. Further research may include a task-performance perception experiment in which observers are required to detect or identify targets in fused images. Presently a set of vehicle images suitable for image fusion is not available. For this reason the more subjective paired comparison test was employed in place of a more objective detection or identification test.

The fusion effort will form another paper for submission to a suitable journal once the perception experiment results are obtained and analyzed.

1.4.4 Planned Future Activities

The active sensor modeling work will be concluded by submitting a paper for journal publication. Other than finishing the writing, the remaining work is to use field data to validate the simulation and proposed simple model. Plans are to submit the paper near the end of the first quarter of year 2 activities.

Perception experiments are planned for the fusion metric effort during August, 2006. The point of the experiments is to help quantify the meaning of the various metrics. That is the metrics will be compared to human observer performance to calibrate the metrics. Once that data is analyzed and incorporated, a paper will be submitted for journal publication probably during the second quarter of year 2 activities.

The image processing techniques modeling will continue during year 2 of Center funding. Intelligence/Surveillance/Reconnaissance (ISR) sensors will be studied to determine which of the imager processing techniques are beneficial to those sensors. Performance modeling for those techniques will then be developed. As for tactical sensors, this will involve perception experiments to validate analytical modeling efforts.

1.4.4 Publications

1.4.4.1 Accepted/Published

K. Krapels, R.G. Driggers, B. Teaney and C.E. Halford, "Handheld threat object identification performance of 2-D visible imagery versus 3-D visible imagery," *Optical Engr.* 45, 063202-1 -9, June, 2006.

D. Tomkinson, P. Richardson, C. Halford, K. Krapels, "Combat smokes in the mid-wave and long wave infrared," *Military Sensing Symposium Proceedings*, Orlando, FL, February, 2005.

S. R. Murrill, E. L. Jacobs, S. K. Moyer, C.E. Halford, S. T. Griffin, F. C. De Lucia, D. T. Petkie, C. C. Franck, "Terahertz imaging system performance model for concealed weapon identification," *SPIE International Conference Proceedings*, vol. 5989, pp. 1E1-1E14, Bruges, Belgium, 2005.

D. T. Petkie, F. C. De Lucia, C. Castro, P. Helminger, E. L. Jacobs, S. K. Moyer, S.R. Murrill, C.E. Halford, S.T. Griffin, C.C. Franck, "Active and passive millimeter- and sub-millimeter-wave imaging," *SPIE International Conference Proceedings*, vol. 5989, pp. 181-188, Bruges, Belgium, 2005.

E.L. Jacobs, R. L. Espinola, C.E. Halford, D. Tofsted, "Beam scintillation effects on identification performance with active imaging systems," *SPIE International Conference Proceedings*, vol. 5987, pp. 031-0311, Bruges, Belgium, 2005.

1.4.4.2 Written, To Be Submitted

K. Krapels, T. Jones, R. Driggers, B. Teaney, and C. Halford, "Target detection in noisy color imagery: Evaluating CIELAB for use in a military target acquisition model,"

C.E. Halford, A.L. Robinson, R.G. Driggers and E.L. Jacobs, "Tilted surfaces in SWIR imagery: Speckle simulation and a simple contrast model," to be submitted to *Optical Engineering*

1.4.4.3 Planned

J.F. Fanning, C.E. Halford, et. al, paper on ATR model

R.K. Moore, C.E. Halford, et. al, paper on fusion metrics with perception experiment results

R.L. Espinola, C.E. Halford, et. al, paper on Laser Range Gated Imager modeling

1.4.5 References

P. Singer and D. Sasaki, "Fully adaptive space-spectral detection of small targets in the absence of a priori knowledge of the spectral signature of the target," *SPIE Proc.* 3809, 1999.

A. Toet and E. Franken, "Perceptual Evaluation of Different Image Fusion Schemes," Elsevier 24, pp.25-37, 2003.

D. Silverstein and J. Farrell, "Efficient Method for Paired Comparison," Journal of Electronic Imaging 10(2), pp.394-398, 2001.

1.5 Milestone - Performance Modeling of Advanced Architecture Systems (Dr. Steven Griffin)

Prior performance models are physics based descriptions of the components and subsystems that form images in the non-terahertz regime. These are generally either infrared (IR) or visual optical modeling systems or electromagnetic field (EMF) based modeling systems in the millimeter wave (mmwave) or at radio frequencies (RF). Though the terahertz (THz) regime has many characteristics in common with these neighboring regions, some aspects are significantly different. After extensive research and a number of meetings, a general approach to THz modeling was established. Prior details were summarized in the three, six, nine, twelve and fifteen month reports. Details of the completion of milestone one, two and three were reported in the progress reports.

This work compliments and enhances existing Army Research Laboratory (ARL) programs by concentrating on selected issues of mutual interest. This includes corrections for deviations from the classical optical performance model descriptions. On the first year proposal cycle, three milestones received particular emphasis.

1.5.1 Modeling of antenna coupled FPA THz detector techniques into existing performance models.

Direct interactions with ARL Maryland and NVESD Virginia have established the current state of the art with regard to antenna configuration, probable focal plane array (FPA) configuration, and performance modeling issues. Components considered included microbolometer arrays, heterodyne sensors (semiconductor / superconductor) with particular emphasis placed on components incorporating arrays of antenna couplers versus those without. The results identified significant differences and causative factors which have been used to make performance modeling recommendations.

In focal plane arrays there is a demonstrated need for antennae as coupling elements. This coupling accomplishes several significant goals. It provides impedance match between free space and the characteristic impedance associated with the THz detectors. Given the relatively poor sensitivity of THz detectors, system designers cannot afford significant signal losses due to impedance mismatch between the optical image and the detector elements. In addition detectors are typically rather small compared to the minimum spot sizes obtainable by THz optics. Microbolometers, for example, perform better as their thermal conductance cross section is reduced driving designs to small, beam lead elevated structures. The minimum THz spot size is typically larger than a wavelength squared. Thus only a small percentage of the optically delivered power falls

on the detector. An antenna is needed to geometrically couple the large spot to the small detector. As in all focal plane arrays, surface area is required to route interconnects on the integrated circuit. Typically antennae are elevated on insulating material and in order to accomplish geometrical coupling are larger than their corresponding detector. This creates surface around the detector that is available for interconnect routing without losing sensitive area at the antennae plane.

Current antenna implementations for focal plane arrays emphasize frequency independent and modifications of frequency independent planar antenna structures. Planar is chosen to ease implementation in the integrated circuit manufacturing process. Frequency independent operation eases design and manufacturing tolerance issues for these extremely high frequencies. Small variations in material properties and dimensional control are not as likely to drive antenna frequency responses out of the range of interest or prevent them from functioning at all. In a typical application, high permittivity material is in close proximity and corrections for high permittivity distortion to antenna gain patterns need to be implemented. In addition the impact of these deviations from the lambertian performance usually incorporated into optical theory need to be considered.

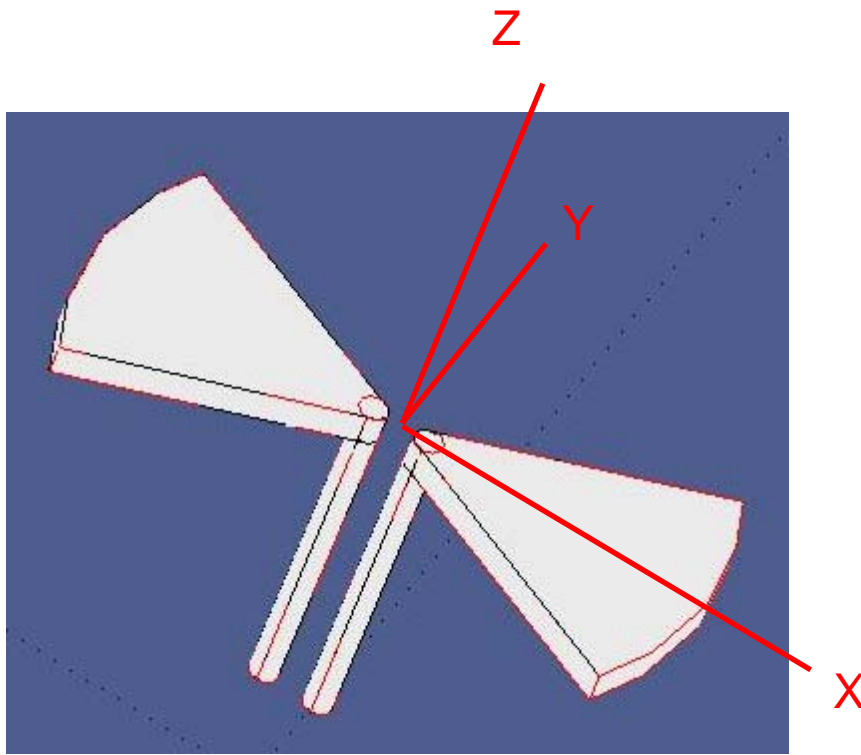
To address the first issue, a survey of current implementations was used to determine common antenna coupling configurations for THz focal plane arrays. These include 2D techniques such as bow-tie or log spiral antennas placed above the corresponding THz detection elements as well as 3D approaches such as semiconductor micro-lens elements formed above the THz detection elements. Representative configurations were chosen from each category including items such as the planar bow-tie and micro-lens which were modeled using both MatLab and FemLab (Comsol). For the purposes here, a bow tie planar antenna (see figure 1.5-1) over high resistance Si was chosen as illustrative of the results. A finite element analysis of the radiation pattern generated was generated.

The simulations used high resistance Si typical of integrated focal plane arrays at 650 GHz. Details of the material performance is limited but available from sources such as [Bolivar,2003]. For this application typical parameters are:

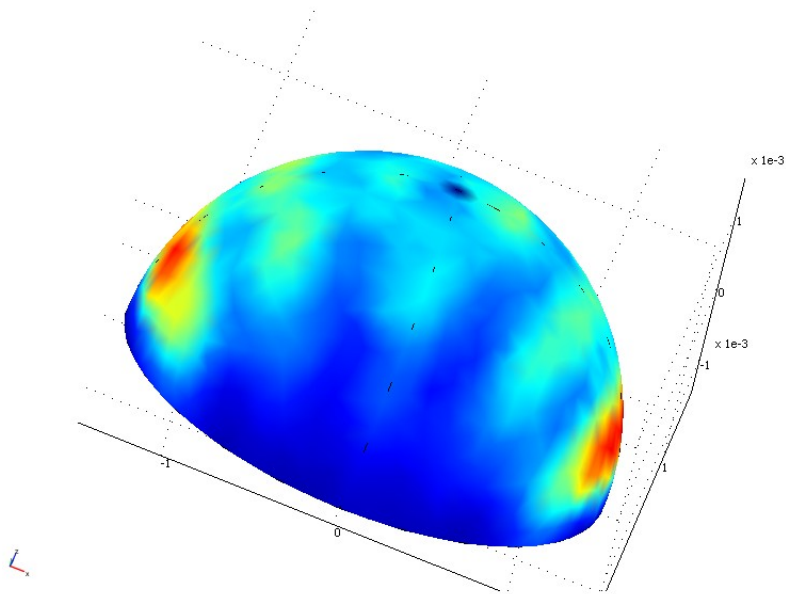
$$\epsilon' = 11.66 \text{ with } \tan \delta = 0.004$$

$$\therefore \epsilon_c = 11.66 - 0.004664j \quad \& \quad \sigma = 1.9 \times 10^{10} \text{ MKS}$$

Slightly less than 100,000 point, boundary condition driven, finite element analysis of antenna radiation problems was used to simulate both the near and far field. Some hand adjustment were made to the mesh to improve the element quality generated by the automated mesh generators. The results were post processed for graphical presentation. Classic free space configurations were used to verify solutions and stability. Additional simulations were run for configurations of interest.

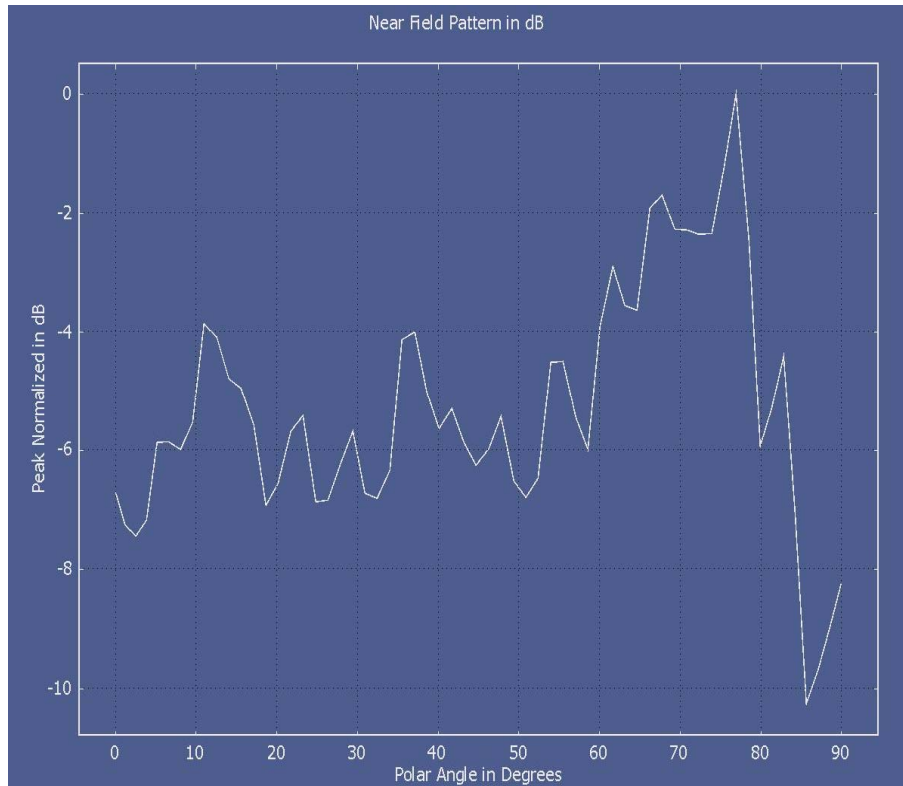


(A)

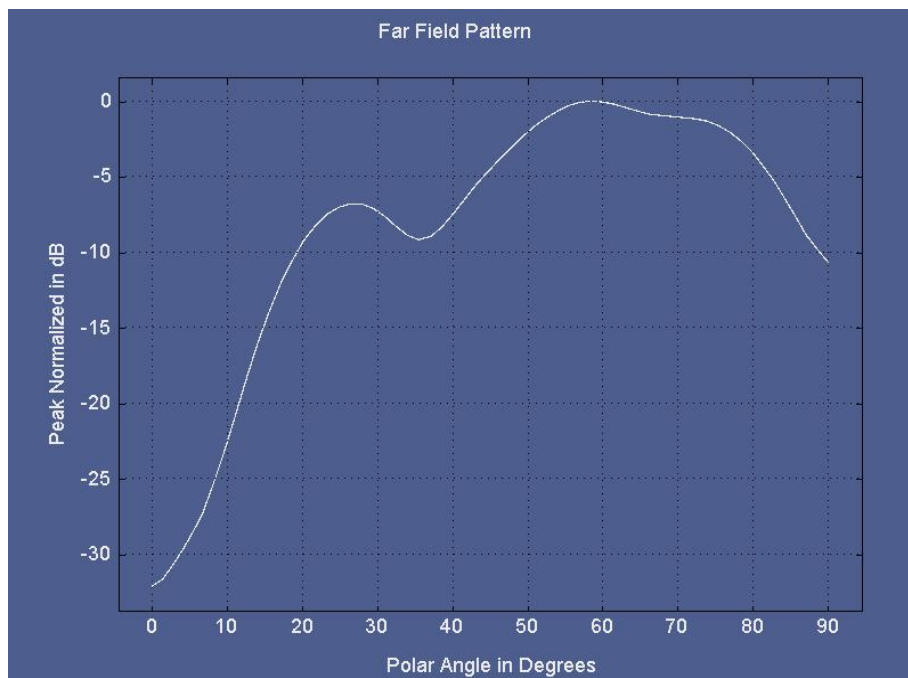


(B)

Figure 1.5-1 Finite Element Analysis of Common THz Coupling Antenna.



(A)



(B)

Figure 1.5-2 Power Flux Density on Near and Far Field Surface as Example of Non-Lambertian Behavior

The results are shown in figure 1.5-1 (B) and figure 1.5-2. To avoid presentation of reams of data a pseudocolor scheme was used in figure 1.5-1 (B) where red indicates a maximum power flux density and blue near zero power density. As can be seen in figure 1.5-1 (B), the 650 GHz emission is modified by the presence of the high permittivity material. Several lobes are observed along the x axis with approximate axial symmetry along the y axis. The usual null is observed at the z axis. What is unusual is the redistribution of the emission (and reception) energy to the lobes closest to the Si surface. Though not clearly visible here, significant power is also being channeled below the Si surface and out the edge of the structure. For each of the figures here detailed numeric files can be provided on request.

In figure 1.5-2, power density emission (reception) are plotted versus a polar angle defined off the z axis along the x axis. In the near field the pattern contains high angular frequency variations typical at ranges where the details of the antenna structure have not smooth out. In the far field pattern, these geometrical details have evened out producing a typical far field pattern except the power density is redistributed to high polar angle values. Even in the near field, the bulk of the energy has been diverted from normal to the surface, to approximately parallel to the surface. This is the usual tendency of high dielectric constant material to concentrate the electric field close to the substrate surface, distorting the usual antenna pattern associated with this antenna type. Though treatments have been proposed in some applications, most focal plane arrays use architectures that make no effort to compensate for the distortion. Even in cases where compensation is applied, the resulting pattern is typically not close to a lambertian pattern assumed by most performance models.

Since standard models tend to assume a lambertian surface behavior and the antenna based THz focal arrays exhibit behaviors far from this, some compensation for the antenna's selective filtering of the spatial frequencies needs to be incorporated. A number of alternatives were considered and a performance modeling technique was proposed, demonstrated and published. As a summary consider the following.

In the traditional Fourier Optical description of an imaging system the lambertian assumption is deeply ingrained in the model and strongly interactive with the paraxial assumption ($\cos \Theta \sim 1$). In antenna based focal plane arrays the higher spatial frequencies traverse the edge of the collecting optics and strike the detector at the largest polar angle; thereby, suffering the greatest relative attenuation. This modifies the effective MTF of the system. In figure 1.5-3 the marginal rays represent the higher spatial frequencies arriving at the detection element at extreme angles. The right most ellipse represents the antenna reception pattern which has the greatest gain on the system's axis of symmetry. This gain attenuates the higher spatial frequency information arriving along the marginal rays, thereby modifying the total effective system MTF from the normal description.

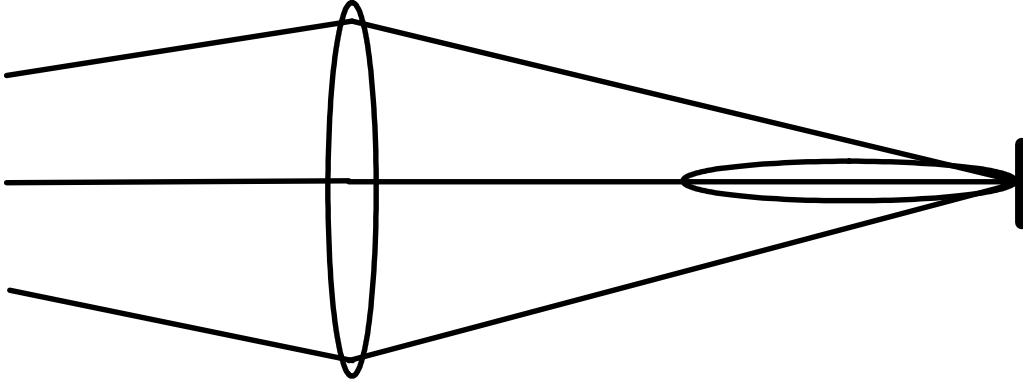


Figure 1.5-3 Diffraction theory modified for use in THz

Interfacing the antenna description into diffraction theory can be accomplished by incorporating the antenna power gain description into the MTF description of an imaging system.

Starting with a classic description: $I \equiv$ Irradiance $H_o \equiv$ Hankel Transform
 $OTF \equiv$ Optical Transfer Function
 $G_a \equiv$ Antenna Gain

For symmetric, clear aperture [GASKILL,1978]:

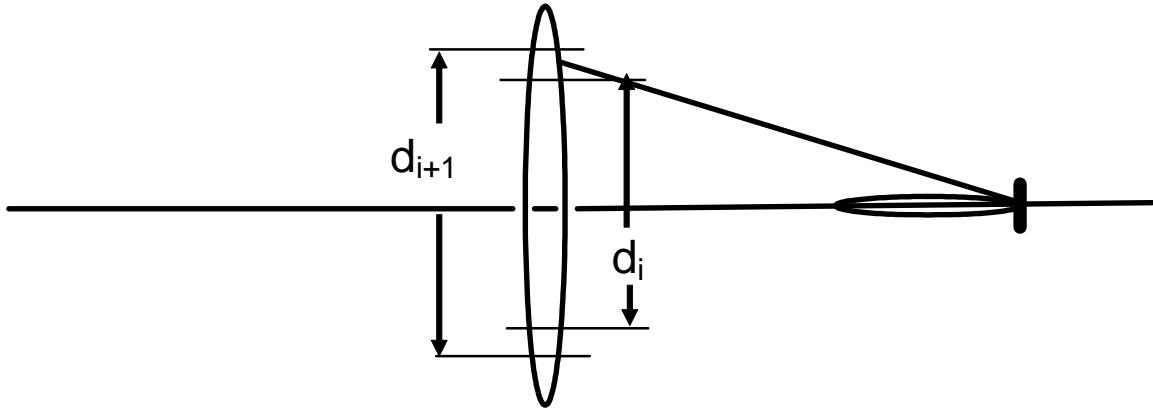
$$I_i(r) = H_o \{ H_o(I_o(r)) OTF(\rho) \}$$

$$I_R(r) = G_a(\theta) H_o \{ H_o(I_o(r)) OTF(\rho) \} = H_o \{ H_o(I_o(r)) [G_a(\theta) OTF(\rho)] \}$$

$$\therefore OTF_R \equiv G_a(\theta) OTF(\rho)$$

To compute the antenna modified MTF – OTF and G_a need to be related.

For symmetric clear aperture $MTF \equiv |OTF| = OTF$.



$\rho_{cj+1} = d_{j+1} / (\lambda l)$ $\rho_{cj} = d_j / (\lambda l)$ $j = \text{lens distance from objective}$
 $G_p = \text{On axis power Gain}$

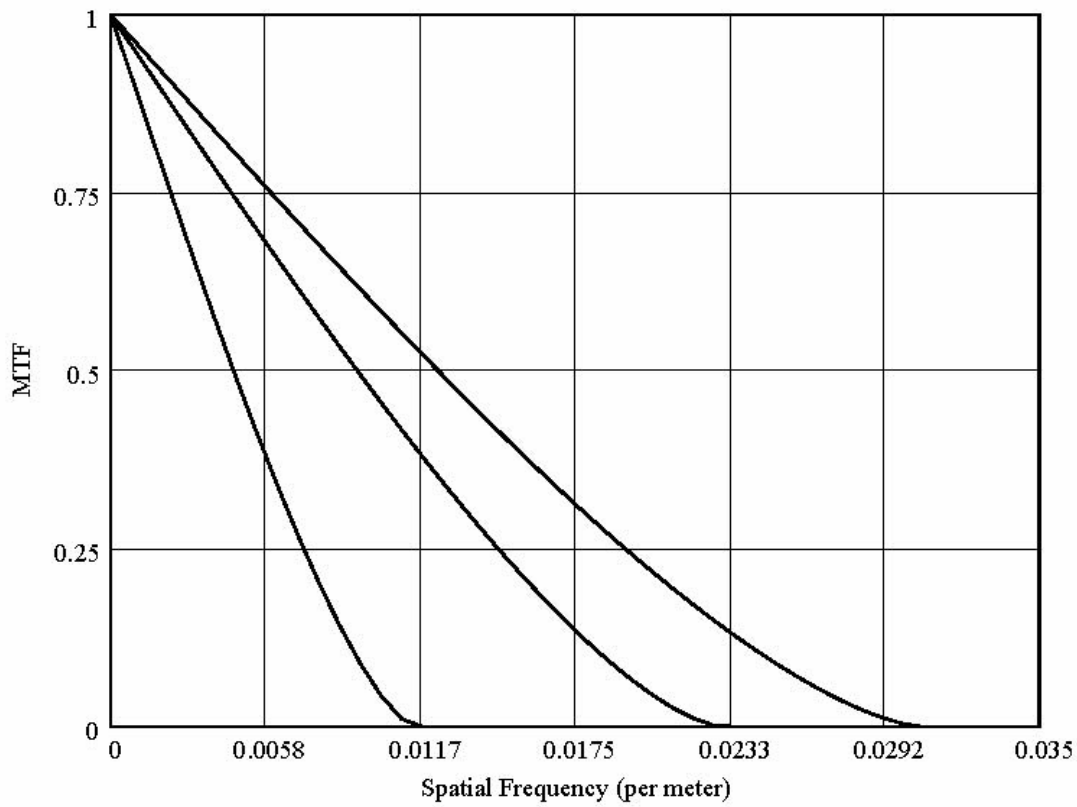
$$MTF_j(\rho) = MTF(\rho; \rho_{c_{j+1}}) - MTF(\rho; \rho_{c_j})$$

Insert into previous

$$I_i = \sum_{j=1}^{N-1} H_0 \left\{ H_0(I_o) \left[G_a(\theta) MTF_j(\rho; \rho_{c_j}) + \frac{G_p}{4} \right] \right\}$$

$$\therefore MTF_R(\rho) = \sum_{j=1}^{N-1} MTF_j(\rho; \rho_{c_j}) G_a(\theta) + \frac{G_p}{4}$$

Modeling in MatLab with the objective cut into 63 distinct annulus plus on axis cylinder yields the MTF curves in figure 1.5-4. Part (A) demonstrates validity for a classic non-aberrating, clear aperture system. Part (B) are examples of the MTF subcomponents to be weighted by the antenna gains at the respective antenna polar angles. The resulting MTF_R (the MTF as received by the antenna) is described above and more accurately describes the effective MTF of a system incorporating antennae at the focal plane. As validation of the model consider figure 1.5-5. In part (A) a classic spatial delta function is presented at the object plane producing the anticipated point spread function at the object for an assumed lambertian antenna reception.



(A) MTF curves for $j=2$, $j=32$ and $j=63$

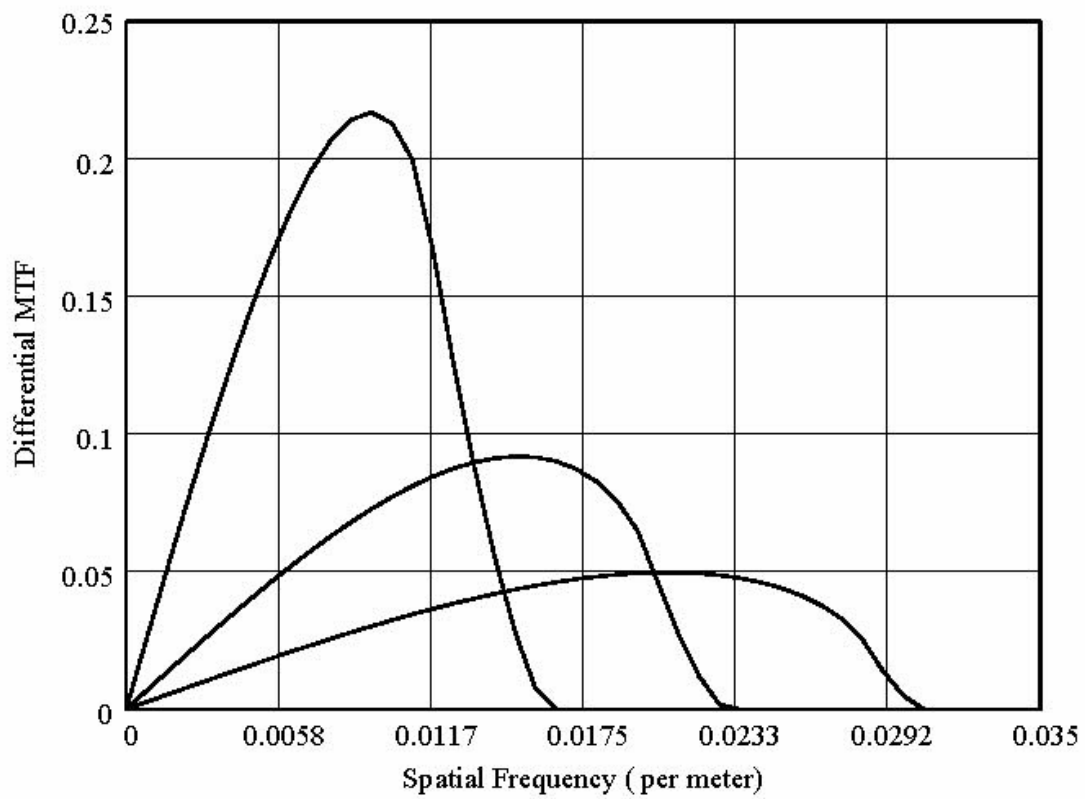


Figure 1.5-4 MTF Optimized for Incorporation of Antenna Pattern

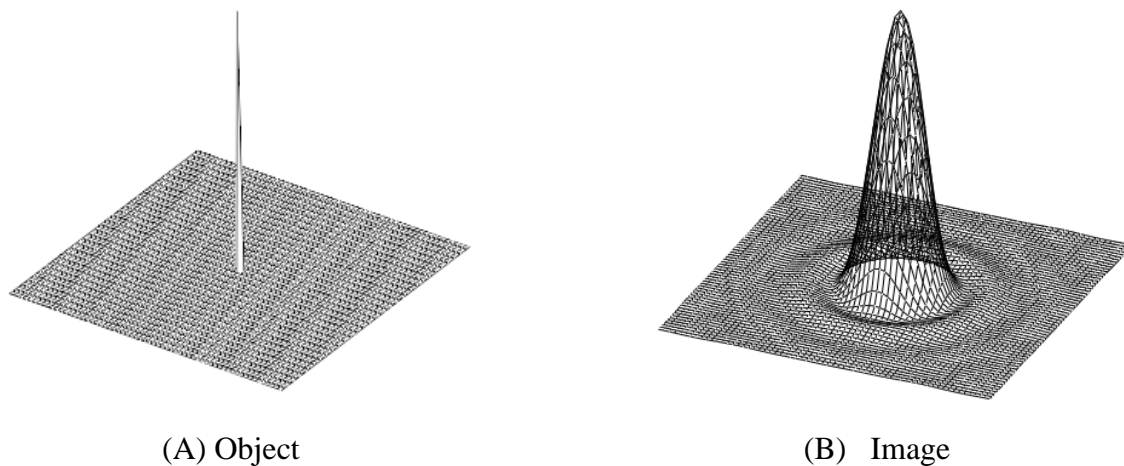


Figure 1.5-5 Antenna Modified Image Simulator Classic Test Case

Specific conclusions for this specific component of the work includes: optical models do require modification for use at THz frequencies even though traditional tests of assumptions are met, the antenna environment anticipated in THz applications needs to be considered in adapting Fourier optics – in particular the interaction between the antenna pattern and the image formation process, a particular modeling adaptation was developed and successfully tested.

In the broader sense, direct interactions with ARL and NVESD have established the current state of the art with respect to antenna configurations, focal plane arrays and performance modeling issues. Particular modifications for performance modeling have been developed and recommended for inclusion in next model revision.

In particular, it was decided that the THz performance model should be divided into a modified radiometric model for use in describing the signal and a modified RF model for use in describing the temporal noise. A diffraction modified radiometric model was used to describe temporal behavior with the antenna modified Modulation Transfer Function (MTF) description of spatial behavior. Technical details were published under separate cover. A modified RF description was used for temporal noise but was found to be limited by the anechoic chamber effect of atmosphere. In this model, performance was described by traditional noise temperature / noise figure descriptions. Spatial noise is dominated by atmospheric interactions via amplitude variations with little phase components. Spatial noise treatment interacted with and led to issues detailed in milestone three.

First milestone was completed August 2005 and reported at six month review.

1.5.2 Support performance modeling of image formation components for THz imaging techniques.

FEMLAB (Comsol) was obtained and implemented. Initial geometric descriptions of a representative image formation configuration have been entered. A traditional optical description of the representative image system has been generated. The principle issues that differentiate the performance of THz wave image formation (collection) optics from behavior typical of the shorter wavelengths have been designated. Imaging at a mission effective “stand off” distance (up to 100 meters) requires a sufficiently long focal length to produce the necessarily small angular subtense for sufficient resolution on target. The field of view of the collection optics is necessarily small. Factoring in practical limitations regarding weight and maximum linear dimensions for the applications envisioned dictates restrictive collection optical diameters.

Modeling was completed for a variety of image formation configurations and comparisons made between traditional optical descriptions (Matlab) and finite element analysis solutions to the complete electromagnetic fields (EMF) solutions (FemLab/Comsol). In particular consider figure 1.5-6. This is an example of a VDI 22dB horn that is integrated into their standard 650 GHz system. In the existing imagers it is placed approximately 1 meter from objective optics. Traditional EMF solutions were extracted from [Johnson,1961]. Traditional optical solutions from [Born,1964]. FEMLAB (COMSOL) finite element analysis solutions were developed for the 22dB horn. The model was validated against the cited standard references and hand calculations. Some manual adjustments were required to the mesh distribution to eliminate numerical simulation artifacts. The numeric results are too voluminous for inclusion here. Selected pseudocolor images are presented for consideration. Additional results available upon request.

In figure 1.5-7 part (A) the power density is encoded with red being maximum and blue being minimum. In part (B) the same information is presented many wavelengths down the appropriate waveguide. The results are consistent with the standard EMF descriptions previously cited. Part (A) is a representation of the TE_{11} mode of this horn. Part (B) is the equivalent for a power detector mounted vertically in a waveguide. Additional hand techniques were used to validate the numerical solutions.

Once model validation was established, results like those indicated in figures 1.5-8 and 1.5-9 were generated. Consider figure 1.5-8. Part (A) is a pseudocolor representation of the power density emitted from a waveguide driven horn. Maximum power densities occur at the waveguide / horn transition and are represented in red. Most of the radiated signal is significantly weaker and is seen in light blue. Examination of the actual numeric data indicate consistency with expected classical patterns. These are represented as a horizontal cross section in part (A). Part (B) is a contrast enhanced version of (A) which brings the weaker fringing fields into view. These can be seen more accurately in the actual numeric data. The principle difference between the classical EMF description and these results are the weak backward propagating fringing fields due to the edge currents at the mouth of the horn. These fields are usually eliminated from the classical solution by assuming far field and approximating them by zero. They would be significant only if

the objective optics / beam splitter of the implementation were so close to the horn as to violate this assumption.

For example see figure 1.5-9. In this case a simple focusing element was placed at the mouth of the horn. The resulting power density is shown with the same pseudocolor representation and is backed by volumes of numeric data. The minimum spot size is demonstrated approximately $\frac{3}{4}$ of the way to the top in part (A). Notice also the high power density intensity (red) in the waveguide due to the standing wave generated by the front surface reflection off the focusing element. In part (B) the contrast enhanced image demonstrates that the fringing fields are appropriately attenuated. Notice also the intensity distribution near the focal point. This appears to be consistent with the classic diffraction limited description [Born,1964] using Lommel functions.

Given the weakness of the fringing fields, it is recommended that they not be considered in the model. However, advantage may be gained from incorporation of Lommel function descriptions into future model revisions. In addition, the close proximity of the objective optics to the horn definitely needs to be addressed. This is partially accomplished by the inclusion of the aperture affect of the objective optics in the radiometric model. A second order correction may eventually be required to model deviations from the ideal horn emission due to coupling between the horn and mirror. This is particularly true if subsequent revisions to the system design reduce the horn to mirror distance.

Second milestone completed October 2005 and reported at six month review.

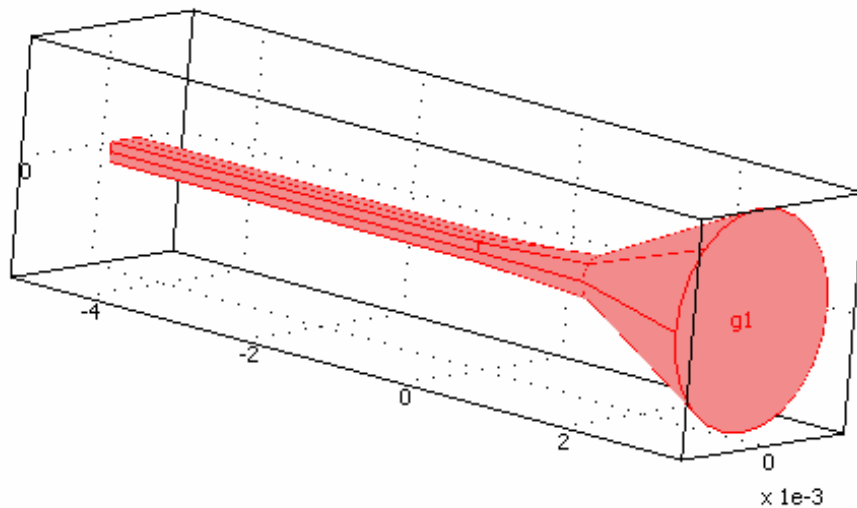
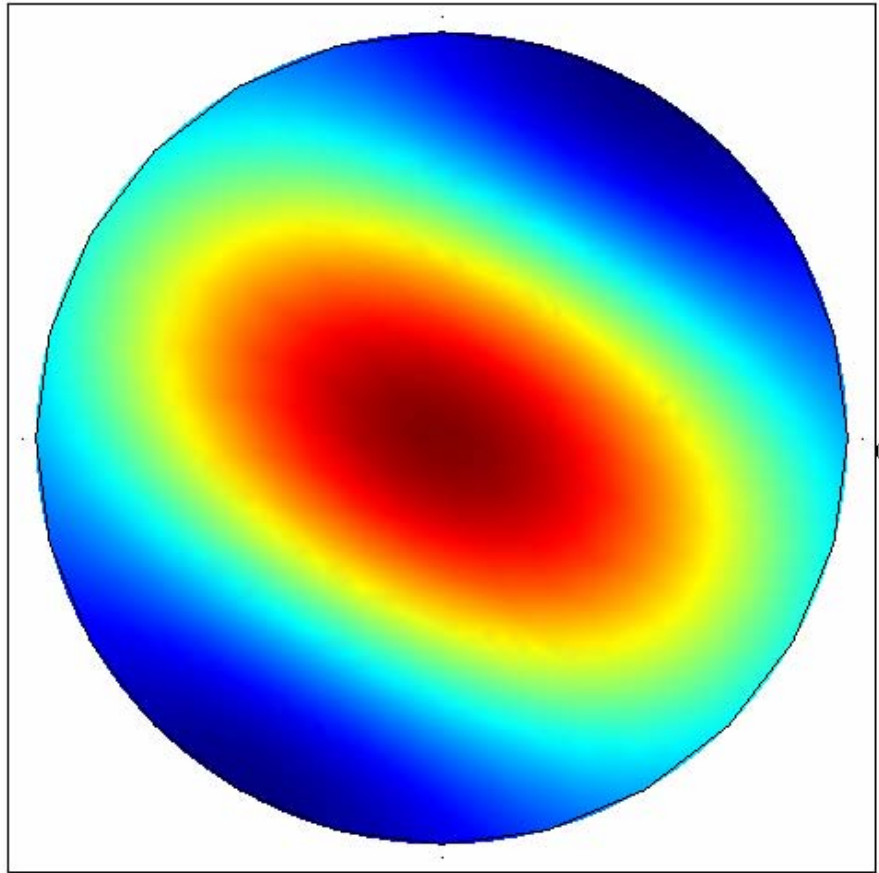
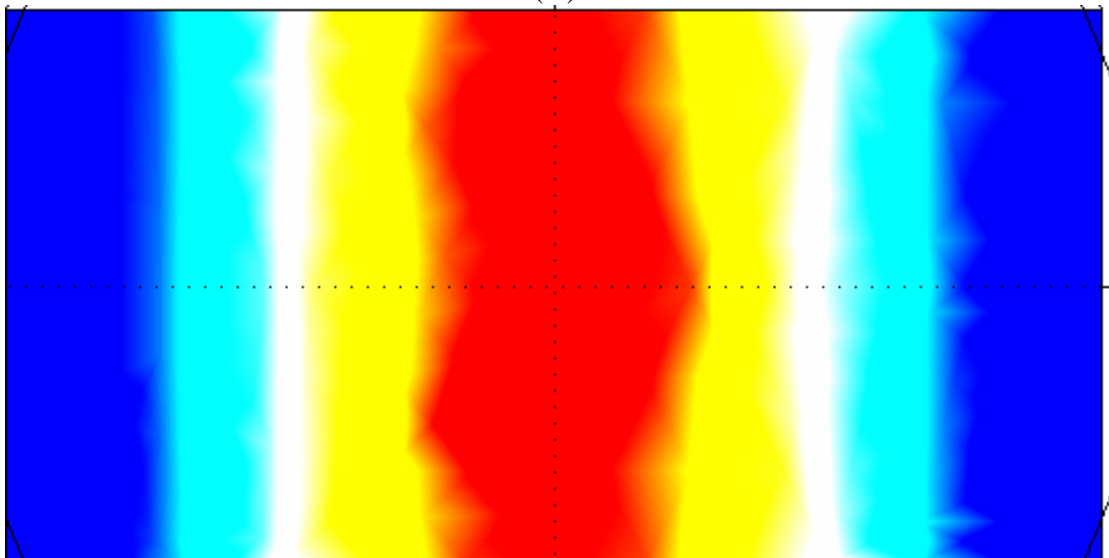


Figure 1.5-6 Example of 22dB Horn

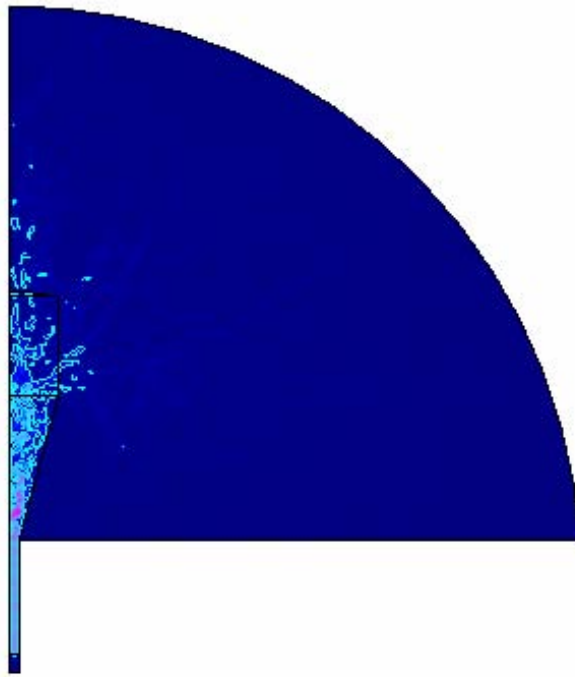


(A)

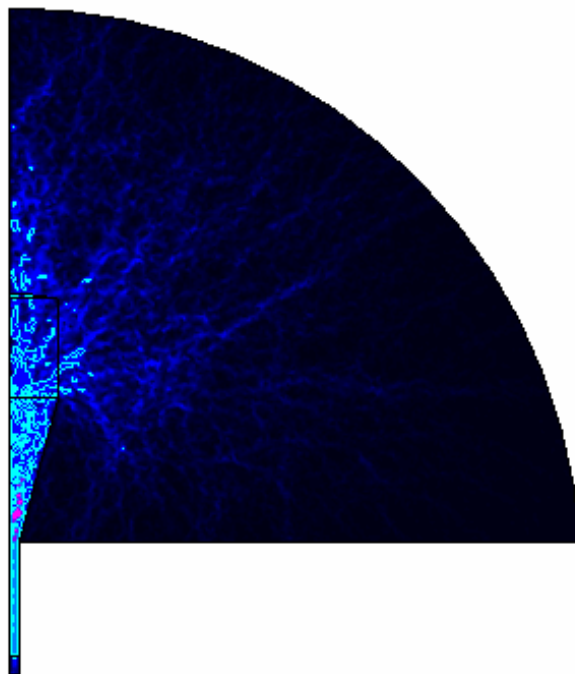


(B)

Figure 1.5-7 TE_{11} Mode in Horn Mouth Neglecting Field Curvature (A) and TE_{11} Mode Deep in Waveguide (B)

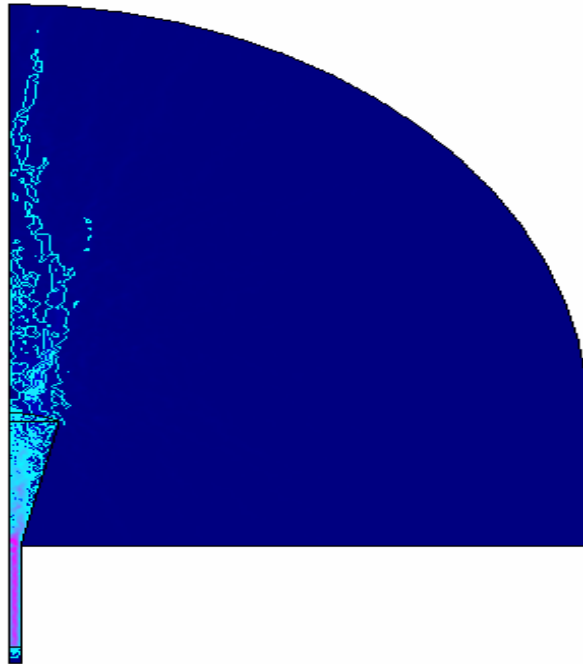


(A)

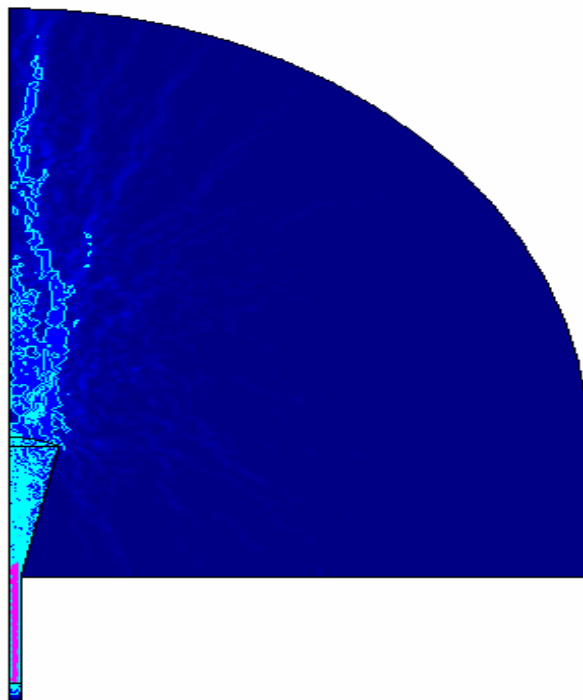


(B)

Figure 1.5-8 Finite Element Analysis of Horn Antenna w/o Focusing Element



(A)



(B)

Figure 1.5-9 Finite Element Analysis of Horn Antenna with Focusing Element

1.5.3 Incorporate THz sensor path and propagation performance modeling.

Non-DOD source THz models have been implemented. These include the performance impact of absorption, scattering and attenuation from the intervening media including air and humidity. Modifications to include turbulence have been researched. Specialized software to model turbulence has been obtained. The research results in this milestone included a modeling review and recommendations leading to future work and follow-on contracts.

1.5.3.1 Non-DOD source THz models were implemented and compared resulting in modeling recommendations

In particular, prior sub-millimeter (millimeter) wave propagation models from non DOD sources were obtained and implemented. Some are summarized in table 1.5-1 below. Though several of the naming nomenclatures address mmwaves, the range of validation includes frequency ranges to 650 GHz and beyond or can easily be extended into this regime. The Liebe model seemed most complete and incorporated much of the other's features. It was originally in Fortran and could easily be modified to accommodate the features of the others. Also the Fortran is still supported on the University of Memphis High Performance Clusters (HPC) and therefore allows the integration of the older code into a newer, more capable platform. These codes model the propagation of THz frequencies through the prediction of scattering, absorption and dispersion and incorporate common molecular species such as diatomic oxygen and water vapor.

Author	Agency	Document Title
Deirmendjian, D.	RAND Corporation.	Far Infrared and Submillimeter Wave Attenuation by Clouds and Rain
Falcone, V.F., Abreu, L.W. and Shettle, E.P.	USAF	Atmospheric Attenuation of Millimeter and Submillimeter Waves: Models and Computer Code
Klein, M. and Gasiewski, A.J.	NOAA	Sensitivity of Millimeter and Sub-millimeter Wave Channels to Clear Air Temperature and Water Vapor Variations
Liebe, H.J.	NTIA	An Atmospheric Millimeter Wave Propagation Model
Liebe,H.J. and Layton, D.H	NTIA	Millimeter-Wave Properties of the Atmosphere: Laboratory Studies and propagation Modeling

Table 1.5-1 Selected THz sensor path and propagation performance models

These results were compared to the existing models at NVESD. Discussions were held at NVESD in conjunction with ARL Adelphi, MD regarding existing models for sensor path and performance modeling. Commonly used models were identified which included the Liebe model enhanced from the sources above. Such models are validated for the

frequency region of interest, see table above, and are effectively implemented in existing performance modeling systems. In a Spring 2006 visit to ARL at White Sands, the performance of the propagation model with regards to turbulence was discussed with ARL personnel. Also performance modeling was conducted under separate contract by the University of Memphis.

As a result it was possible to compare and contrast the performance modeling issues considered most significant. In particular, traditional views of absorption and scattering were revised to more effectively incorporate the dominant factors in the THz region. Traditional RF noise considerations were mitigated by the presence of a low energy, anechoic chamber effect due to the opacity of the atmosphere at these frequencies. Some minor technical adjustments had to be made to the details of the statistical analysis. For example the modification of the statistical description of noise due to the photon energy being small compared to the thermal energy; however, these corrections were generally over whelmed by the atmospheric opacity and low emission level. Current implementations emphasize coherent (Super heterodyne) detection in order to improve the sensitivity of existing commercially available THz sensors. With the gain and phase sensitivity of these approaches, temporal noise due to propagation does not appear to be a limiting issue.

However, turbulence represents a unique challenge for propagation related image performance modeling which is not addressed by propagation models such as Liebe. Liebe's model tracks longitudinal (temporal) effects of the propagation path which though related to the affects of turbulence is tied to them in a computational intensive manner. For more effective implementation, turbulence needs to be tied to the lateral (spatial frequency) aspects of image performance modeling.

1.5.3.2 Specialized Software

Specialized software to model turbulence has been obtained. GUI driven commercial packages such as FLUENT were obtained and investigated. An example of an application is shown in figure 1.5-10, which is a 3D CAD description of the University of Memphis campus. Such results generally rely on Navier-Stokes style descriptions of flow under boundary conditions with enhancements for Kolmogorov based turbulence. Critical parameters such as inner and outer scale or viscous dissipation limits are arbitrarily set by the programmer. Though effective for illustrative purposes, this degree of adjustment limits effectiveness for prediction.



(A)



(B)

Figure 1.5-10 Traditional Turbulence Simulation

1.5.3.3 Modifications to include turbulence have been researched.

Traditional approaches to modeling the impact of turbulence on image formation for THz as well as the higher optical frequencies emphasize a three step technique. The first step is to predict the distribution of velocity and pressure fields from descriptions of material properties and boundary conditions. Secondly to propagate an electromagnetic signal through the results of step one to predict the impact of small optical property variations on the amplitude and phase of the radiation. Finally this result is integrated into the description of the image via spatial frequency representations or equivalent. Each is considered in turn.

Step one may be approached through the simulation of dynamical systems [Frish,1995] described by Navier-Stokes.

$$\frac{\partial \vec{v}}{\partial t} + \vec{v} \cdot \vec{\nabla} \vec{v} = -\vec{\nabla} p + \nu \vec{\nabla}^2 \vec{v} + \vec{f}$$

$$\nabla \cdot \vec{v} = 0$$

plus I.C.and B.C.

Unfortunately Kolmogorov's k-Theorem regarding uncomputability limits the effectiveness of this [Vulpiani,2003]. Various approaches involving assumptions or approximations have been historically applied to this problem which can be broadly grouped [Stanisic,1988] into four principle thoughts Komolgorov, Heisenburg, Kraichman and Hoff. The details are not of principle interest here. All represent significant insights and all have acknowledged limitations.

The principle limitation from a performance model perspective spans all of them and addresses the basic three step approach outlined above. It generates large quantities of unnecessary information regarding the molecular mechanics and EMF behavior. What is really desired here is to determine the affect of turbulence on the propagation of a spatial frequency component of an image. Without turbulence the propagation is the quadratic phase factor. Deviations from it in a turbulent atmosphere represent the effect of turbulence. What is required from a performance modeling standpoint is a description of the impact on a single spatial frequency of propagating through a turbulent atmosphere without engaging the three step process above. Details of this are being developed in a follow-on effort.

1.5.3.4 Conclusion

A result of the comparison and contrast of the propagation performance models indicates a number of issues of significance from turbulence. These were developed from the comparison of ARL White Sands, ARL Adelphi and NVESD efforts. Firstly the impact of humidity variations across the eddies (turbules) present in boundary layer flow at the surface is particularly effective at phase shifting and attenuating the THz frequencies. This introduces spatial variations in potential THz images due to differing propagation paths. The spatial noise introduced has significant impact on the performance modeling in the THz regime. Incorporation of this into a general performance model is hindered by the molecular mechanistic orientation of prior modeling. Prior descriptions of turbulence have emphasized Poincare, Navier Stokes, Kolmogorov, Chaotic Theory, etc. These approaches are oriented towards the development and understanding of molecular motion as it relates to classical dynamical descriptions. For the purposes here, it is the interaction of the molecular dynamical field with the electromagnetic image information that matters. The classical description tends to include a great deal of detail that is extraneous and is cast in manner that is mathematically awkward for the calculation of image performance. In consultation with ARL Whites Sands and New Mexico State a need for a more compact model for incorporation into the description of the imaging process was identified. This was perceived as the most significant performance modeling issue identified in completion of milestone three of the year one effort. In a follow-on effort (Summer 2006), model components are being converted to a high performance cluster at the University of Memphis.

The third milestone was completed April 2006.

1.5.3.5 Future work

For future development, emphasis will be given to the modeling techniques originally developed by Heisenberg. These emphasized the energy cascade from large eddies to smaller eddies at the expense of mechanical details incorporated into the classical descriptions. Such an approach can be more economically integrated into performance models while preserving the essential elements for performance accuracy. Such a change in modeling emphasis should reduce computation requirements and result in more engineering effectiveness for the predictions. Follow-on research has been pursued with the intention of obtaining separate funding to support the further development of this. Team members have been contact and agreed in principle. A preliminary model has been developed to support proposal efforts.

Publications and additional proposals have been made and received as a result of this contract. Follow-on research has been suggested by these results. New interactions with ARL at White Sands, NVESD at Ft. Belvoir, RTTC at Redstone and ONR have been developed. Dr. Griffin would like to thank the sponsor for this opportunity.

1.5.4 Publications

1.5.4.1 Accepted/Published

S.T. Griffin, “Terahertz Image Plane Antennae”, IEEE 2006 International Workshop on Antenna Technology, 06EX1191C, pp. 428-431, White Plains, NY, 2006.

S.R. Murrill, E.L. Jacobs, S.K. Moyer, C.E. Halford, S.T.Griffin, F.C. DeLucia, D.T. Petkie, C.C. Franck, “Terahertz imaging system performance model for concealed weapon identification,” SPIE International Conference Proceedings, vol.5989, pp.1E1-1E14, Bruges, Belgium, 2005.

D.T. Petkie, F.C. DeLucia, C. Castro, P. Helminger, E.L. Jacobs, S.K. Moyer, S.R. Murrill, C.E.Halford, S.T.Griffin, C.C. Franck, “Active and Passive millimeter- and submillimeter-wave imaging,” SPIE International Conference Proceedings, vol. 5989, pp. 181-188, Bruges, Belgium, 2005.

1.5.4.2 Planned

Griffin, S.T., “Incorporation of Antenna Non-Lambertian Angular Dependence into Optical Radiometric Models”, IEEE Transactions on MTT, paper on impact of non-lambertian antenna patterns on performance modeling

S.T. Griffin, C.E. Halford, and S.R. Murrill, “Modifications to Radiometric Performance Modeling for the THz”, Optical Engineering, paper on differences between standard optical and THz

1.5.4.3 References

Total bibliography exceeds 210 entries and is available upon request.

P. Bolivar, M. Brucherseifer, J. Rivas, R. Gonzalo, I. Ederra, A. Reynolds, M. Holker, and P. de Maagt, “Measurement of the Dielectric Constant and Loss Tangent of High Dielectric-Constant Materials at Terahertz Frequencies,” *IEEE Trans. MTT*, 51, pp. 1062-1066, 2003.

M. Born and E. Wolf, “Principles of Optics,” Pergamon Press, pp.370-455, 1964.

U. Frish, “Turbulence: The Legacy of A.N. Kolmogorov”, Cambridge University, pp. 27-39, 1995.

J. Gaskill, “Linear Systems, Fourier Transforms, and Optics,” John Wiley & Sons, pp. 497-506, 1978.

R. Johnson and H. Jasik, “Antenna Engineering Handbook, 2nd ed”., McGraw-Hill, pp. 41-9 – 41-11, 1961.

M.M. Stanisic, “The Mathematical Theory of Turbulence”, Springer-Verlag, pp.162-250, 1988.

A. Vulpiani and R. Livi, “The Kolmogorov Legacy in Physics”, Springer-Verlag, pp. 1-50, 2003.

2.0 Vanderbilt University - Program in support of the Center for Advanced Sensors, Year 1 Annual Report

2.1 Administrative

This project supports the mission of the CAS to develop a fundamental understanding of the interplay between nanotechnology and bio-electronics with intelligent imaging sensor architectures and an intelligent sensor infrastructure. Within this multi-university, multi-year effort, Vanderbilt University has the following tasks:

1. Relate Natural Vision to Night Vision Signal Processing – the Bio-Optics of Vision

Research natural (living organism) optical sensory representation by neural assemblies, recording isolated neural activity across a network of cells. Determine the coding of visual signals by cell populations and achieve a working view of the neural code to achieve superior electronic approaches to rapid AI night vision image signal processing

2. Develop Diamond Bio-electrodes

Develop diamond-based, monolithic multi-microelectrode array for in vivo recording and micro-stimulation

3. Develop Advanced IR display

Research nanotechnology capabilities for enhancing imaging sensor performance, including advanced high definition infra-red displays

The Vanderbilt Program in support of the Center for Advanced Sensors is on schedule and spend plan. This report summarizes and describes the Year 1 progress for the CAS.

2.2 Bio-Optics of Vision – Professor A.B. Bonds

2.2.1 Statement of Purpose

Our global goal is to develop a clear understanding of how the brain detects visual structure. This information can then serve as a substrate for biologically-plausible models for pattern discrimination to achieve superior electronic approaches to rapid AI night vision image signal processing. Our fundamental innovation is to examine how cooperation between cells in the visual cortex enhances the overall amount of information that is available for discrimination. Traditional models rely mainly on the information contained in the firing rate/output magnitude of individual cells/visual filters. We have found that joint analysis of the firing patterns in populations of neurons adds information (beyond the independent analysis), supporting higher levels of discrimination of structure and detail. The fundamental mechanism for intercellular cooperation is firing synchrony, within a 10 msec window (2.2 - 1). We have therefore undertaken a series of experiments to determine the specific visual conditions that encourage synchrony and whether the resulting synchrony enhances visual discrimination (provides *emergent* information) beyond that which is available from the firing rate (filter output magnitude).

We have subdivided this effort into two basic investigations: (1) Study of responses to analytical stimuli (gratings, noise patterns) to understand the fundamental spatiotemporal relationships that underly the generation of synchrony, and (2) study of responses to natural stimuli to elaborate the specific visual structures that synchrony can

discriminate. The fundamental model for investigation is the primary visual cortex (Area 17) of the anesthetized cat, into which we insert a 10 x 10 (total 100) electrode array. This typically yields discriminable single-unit activity from 60-70 cells simultaneously. Synchrony between cell pairs is determined using the Joint Post Stimulus Time Histogram (2.2 - 2). Synchrony between larger groups of cells is quantified using a unique method that we have developed during the previous project period (see below).

2.2.2 Summary of results.

(1) *Initial contact and discussion.* We attended a project meeting at Ft. Belvoir VA in October 2005. This led to some discussion of interfacing of our work with other ongoing efforts. Dr. James Sumner forwarded a copy of our report to Rene dePontbriand, Associate Director of Research ARL-HRED. He in turn has referred us to both Grayson Cuqlock-Knopp and Bill Monaco, both senior vision researchers at HRED. Discussions are ongoing. (2) *Sensitivity of synchrony to fundamental visual structures.* We find that synchrony is more sensitive than firing rate to the degree of coherence of strictly motion-defined structures. (3) *Development of multicell coherence quantification method.* We have developed and exhaustively tested a means of characterizing both the quality and quantity of interactions in populations of 3 or more cells. (4) *Sensitivity of synchrony to natural image qualities.* We have tested the relative sensitivity of both synchrony and firing rate to three types of image degradation: Noise, blur and contrast reversal. Neural synchrony was much more sensitive to changes in noise and blur than was firing rate. Neither synchrony nor firing rate were significantly affected by contrast reversal. (5) *Selectivity of synchrony within cell assemblies to natural images.* We find that synchrony within assemblies of up to ten cells are highly selective to specific images within a sample of 4500 natural images. This implies that synchrony is a reliable substrate for sparse coding of particular image properties. Early results suggest that synchrony is a vector for signaling contour integration, and that the selectivity reflects specificity for particular contours.

Significance. These results collectively imply that while firing rate (filter output magnitude) conveys information on the fundamental structure of images, **synchrony provides more information on image details, e.g., edges and contours.** This suggests that **cooperation between filtering elements is necessary for optimizing discrimination of fine image structure, especially in conditions of masking by noise and blur.**

Benchmarks, 2006-2007. 1. Contour integration by synchrony. We will characterize the reliability of contour integration by synchrony and determine how it is affected by natural interference such as noise, blur and contour occlusion. 2. Impact of image qualities on synchrony. We will test how spatial phase and frequency information and high-pass filtering modify synchrony and firing rate. 3. Coordination of synchrony with the association field. Association field theory (2.2 - 3, 4) links behavioral discriminability with the statistics of natural images. We will seek similar links between the statistics of natural contours and synchrony in the visual cortex.

2.2.3 Specific results

1. *Synchrony dependence on motion coherence* (2.2 - 5). As a first test of the involvement of motion coherence and synchrony, we have found that synchrony detects

structures generated purely by motion. We compared synchrony from drifting sinusoid gratings and moving dot patterns. For dot stimuli, 10% of the dark background was covered by randomly distributed bright dots. In "figure" regions consisting of periodic bars of the same spatial frequency as the gratings, some of the dots drifted coherently, while all remaining dots both inside and outside these regions moved in random directions. The figure regions themselves moved at the coherent drift rate, creating the perception of a drifting grating pattern. 203 cell pairs showed synchrony under drifting grating stimulation, and of these 63 cell pairs showed synchrony under random dot stimulation. For those pairs, a Student's t-test revealed that the synchrony amplitude for a random dot stimulus with 100% coherence is lower than that for the drifting grating stimulus ($P < 0.001$) but higher than that for the dot stimulus with 70% coherence ($P < 0.001$; Fig 2.2 - 1).

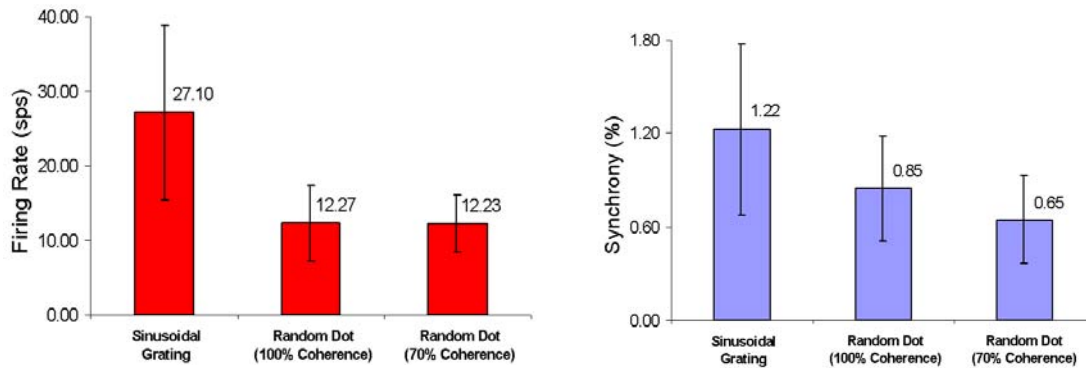


Figure 2.2 - 1 Sensitivity of synchrony (left) to dot coherence

The average firing rate for drifting gratings was twice that from random dot stimuli with 100% coherence, but the average firing rate for dot stimuli with 100% coherence did not differ significantly from those with 70% coherence ($P > 0.01$; Fig. 2.2 - 1, bottom). Synchrony detects temporally correlated structure even without clearly defined contours, but spatial integrity increases the synchrony strength. Synchrony, but not firing rate, is sensitive to the coherency level of temporally correlated structure.

2. *Synchrony in larger assemblies.* Cross-correlograms (2.2 - 6) and techniques such as the JPSTH (2.2 - 2) cannot characterize the synchrony between more than two cells. The cross-correlogram has been extended to include cooperation among three cells (2.2 - 7, 8), but the resulting display cannot be applied practically to larger groups. Gravitational clustering (2.2 - 9, 10) identifies cells that fire together, but results are qualitative and still based on pairwise distance calculations. To quantify cooperation within multicell assemblies, we have developed a method that will detect and quantify the amount of correlated activity in a large ($n \geq 2$) cell assembly. A fixed integration window is inappropriate for comparisons across larger groups, so our basic algorithm is designed to reflect the relevance of group synchrony to post-synaptic neurons by modeling the summation of postsynaptic potentials (PSPs).

By convolving a point-event spike train with a truncated (10 msec.) alpha waveform (yielding a PSP train), we derive a similarity measure that is conscious of time (Fig 2.2 - 2). PSP trains for a group of cells can be summed and filtered to identify spike times that are coincident above a threshold. The *Quantity* of synchrony is computed as the ratio of

the area under coincident waveforms to the total area under all waveforms in the assembly. The *Quality* of synchrony is an index computed on the basis of the average overlap of coincident waveforms and the length of time a group cooperates. Unlike other approaches, this can be applied to neural assemblies of arbitrary size, not just pairs. This algorithm also selectively emphasizes spikes that occur closely in time instead of treating all spikes within the integration time period as equally important events. To examine characteristics of group membership, we can resolve and compare individual contributions. Also, by using shuffle and shift predictor techniques (2.2 - 6), we can resolve and separate sources of synchrony, i.e. cooperative activity stemming from endogenous

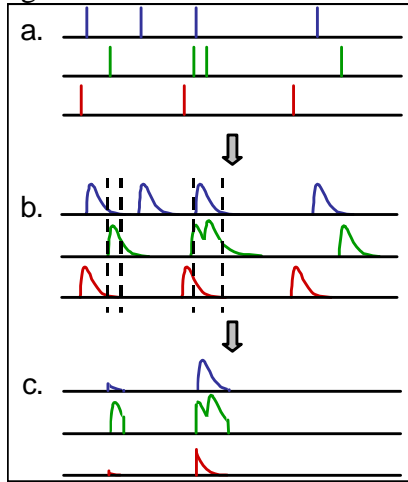


Figure 2.2 – 2 Schematic of similarity measure. (a) Spike trains from 3 neurons in an assembly. (b) PSP trains created by convolving each spike train with an alpha function. (c) Each PSP train is filtered to preserve only portions of waveforms that are coincident above a threshold.

sources, stimulus effects, and firing rate-induced modulation of synchrony.

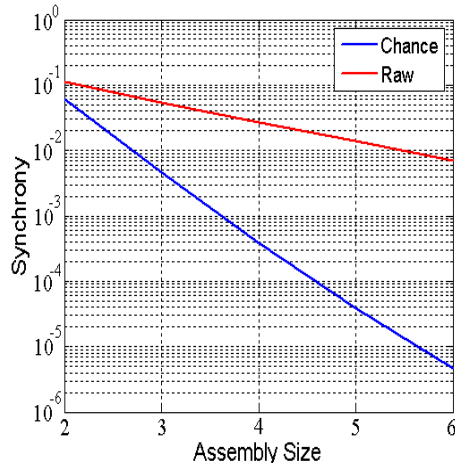


Figure 2.2 - 3 Raw vs. chance synchrony measured from subsets of 39 cells when viewing a natural image.

Chance synchrony was calculated by averaging shift predictors computed for 200 randomly chosen assemblies in each size group. On average, significant assemblies of 6

We compared results from spike pairs using this method against the JPSTH method (2.2 - 2) and identified not only the same pair assemblies, but also others, most likely due to the use of temporal weighting (as opposed to fixed binning). The uncertainties of normalization and firing rate dependence are minimized due to the very large ratios seen between chance and observed probabilities of synchrony as group sizes grow (Fig. 2.2 - 3). Observed synchrony was calculated by averaging raw scores for 39 significant assemblies per size group.

cells contain 1500x more synchrony than that expected by chance (2.2 - 11). This method is advantageous because: (1) It can be applied to an arbitrary number of cells. (2) Waveform parameters like PSP amplitude, integration time and threshold are adjustable. (3) The spike trains from excitatory and inhibitory cells can both be represented (an IPSP train results from convolution with a negative alpha function). (4) We can normalize synchrony scores by subtracting the shift/shuffle predictor to associate coordinated events with specific sources of synchrony. For instance, firing rate effects can be removed and analysis can be based on endogenous and stimulus-induced synchrony, or firing rate and stimulus effects can both be removed and the analysis can focus on synchrony from only endogenous sources. (5) Members of large groups can be predicted from the scores of smaller groups, thus drastically reducing the number of group permutations that need to be computed. (6) No binning or smoothing techniques are required. (7) This method is based on biological principles and the results are physically meaningful (i.e. a score of 0.15 means that 15% of all waveforms in a group were coincident).

3. *Synchrony dependence on natural image manipulation* (2.2 - 12). One challenge in analyzing synchronous responses to natural stimuli lies in linking response changes to a specific stimulus attribute. To investigate the properties of natural stimuli that encourage assembly formation, we conducted differential measurements. One manipulation was to measure a response to a control image and then modify the image by noise addition. We recorded from 210 groups of neurons (42 groups of 2-6 cells each).

Five natural images, jittered by $<0.5^\circ$ for two secs, were degraded in five steps (Fig. 2.2- 4). Cooperative responses were compared to those from the original image and

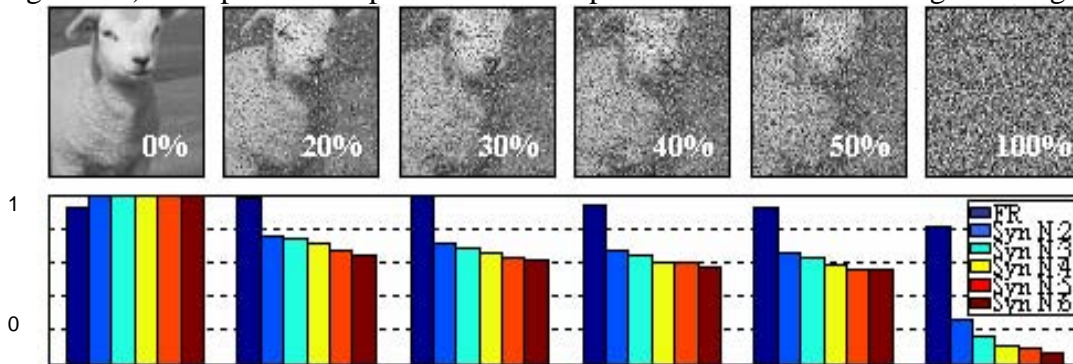


Figure 2.2 - 4 Responses to five different levels of noise degradation. Both firing rate (FR) and synchrony are normalized to 1, and vertical scale is linear. Colors represent relative synchrony of different group sizes (n=2-6)

the difference represented the consequences of the imposed modification. For 50% noise, synchrony decreased 33.8% for pairs and 44.2% for 6-cell groups ($p < 0.004$) though average firing rates (FR) did not change significantly ($p > 0.05$). Synchrony is only destroyed by complete elimination of structure. For both noise addition and low-pass filtering, synchrony is reduced much more strongly than is firing rate, and synchrony is sensitive to the degree of modification, unlike firing rate. We found no significant change in either response property for contrast reversal, indicating that synchrony, like firing rate, shows non-linear rectification in complex cells. From these preliminary observations **we hypothesize that while firing rate signals the fundamental structure**

of the image, synchrony transfers information on fine detail, which is disrupted either by noise or low-pass filtering. We do predict that synchrony will be less disrupted when images move behind noise, since the overall image structure is still present. These results would be consistent with our earlier finding that synchrony signals fine, but not coarse, changes in orientation (2.2 - 1). On this basis we expect that synchrony will be less disrupted by high-pass filtering and preservation of phase information, which carries energy in detail, and that both firing rate and synchrony will be severely reduced by elimination of phase information, which defines the image structure.

4. Selectivity to natural images. To investigate the relative merits of encoding by firing rate or cooperation within neural assemblies during natural vision, we compared the selectivity of average firing rate and synchrony of cortical cells exposed to a sequence of 4500 natural images. Using a 10x10 microelectrode array, we recorded from 71 complex cells in the primary visual cortex of two paralyzed and anesthetized cats. We randomly identified (without regard to spatial selectivity or RF location of members) 350 neural assemblies, ranging in size from 2 to 8 cells with 50 assemblies per size group. We used the fourth moment (excess kurtosis) of the response distribution as a measure of selectivity for each assembly. Response distributions with a large kurtosis are more selective in that they have a high probability of a weak response and a low probability of a strong response for any single image in the sequence. Therefore, an assembly whose response distribution is highly leptokurtic (excess kurtosis > 0) will respond strongly to only a few images in the sequence and is thus more selective. We measured the synchrony and average firing rate response distributions for each assembly over the set of images and found that all distributions were leptokurtic, but synchrony response distributions were highly leptokurtic and kurtosis increased nearly exponentially with assembly size. On the other hand, the kurtosis for average firing rate response distributions stayed relatively constant across assemblies of different size. Synchrony was 3.9 times more selective than average firing rate for pairs of cells and 302.4 times more selective for assemblies of 8 cells. These results suggest that synchronous activity among neural assemblies is more selective than average firing rate in the context of natural images. Increasing assembly size enhances the ability of synchronous coding to

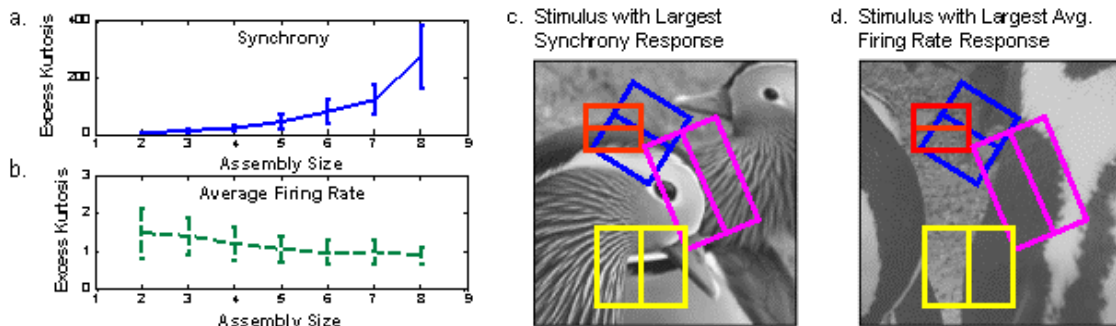


Figure 2.2 - 5. The kurtosis (selectivity) of synchrony response distributions (a) increases nearly exponentially with assembly size, but (b) remains constant for firing rate distributions. (c) Example where the aggregate receptive fields for a given assembly lie along a complex contour in the image with the best synchrony response, but (d) follow no particular structure in the image with the best average firing rate response.

discriminate, but there is no information gain for average firing rate when additional cells are considered. We propose that higher-order features found in natural images (e.g. complex contours) are responsible for the high selectivity of synchrony compared to average firing rate because adequate descriptions of high-order spatial correlations require the coordinated response of multiple cells. This process is cumulative, in that more complex structures require larger neural assemblies for accurate description.

We also note that there was a tendency for the images that generated the most synchrony in a group to have continuous contours along the lines of the receptive field preferences (Fig. 2.2 - 5c, above). **This suggests that synchronous assemblies are important to the process of contour integration.** We will explore the reliability of this result in future experiments.

2.2.4 Publications

1. Bernard, MR, Zhou, Z & Bonds AB. Synchronous activity in cat visual cortex detects structural modifications in natural images. Vision Sciences Society, Sarasota FL May 2006.
2. Zhou, Z, Bernard, MR & Bonds, AB. Synchrony modulation in cat visual cortex reflects structure from coherent motion of random dots. Vision Sciences Society, Sarasota FL May 2006.
3. Bernard, MR, Zhou, Z & Bonds AB. Synchrony in Cat Visual Cortex is More Selective for Natural Images than Average Firing Rate. AREADNE Conference (Research in encoding and decoding of neural ensembles) Santorini Greece, June 2006.
4. Zhou, Z, Bernard, MR & Bonds, AB. Spatial coherence of visual stimuli modulates synchronized activity in cat visual cortex. AREADNE Conference, Santorini Greece, June 2006.

2.2.5 References

1. Samonds JM, Allison JD, Brown HA & Bonds AB. Cooperation between Area 17 neuron pairs enhances fine discrimination of orientation. J Neurosci. 23:2416-2425, 2003.
2. Aertsen AMHJ, Gerstein GL, Habib MK & Palm G. Dynamics of neuronal firing correlation: Modulation of "effective connectivity". J. Neurophysiol., 61:900-917, 1989.
3. Field DJ. What the statistics of natural images tell us about visual coding. Proc. SPIE. 1077:269-276, 1989.
4. Field DJ, Hayes A & Hess RF. Contour integration by the human visual system: evidence for a local "association field". Vision Res. 33:173-193, 1993.
5. Zhou, Z, Bernard, MR & Bonds, AB. Synchrony modulation in cat visual cortex reflects structure from coherent motion of random dots. Vision Sciences Society, Sarasota FL May 2006.
6. Perkel DH, Gerstein GL & Moore GP. Neuronal spike trains and stochastic point processes, II. Simultaneous spike trains. Biophys. J. 7:419-440, 1967.
7. Perkel DH, Gerstein GL, Smith MS & Tatton WG. Nerve-impulse patterns: a quantitative display technique for three neurons. Brain Res. 100:271-296, 1975.
8. Abeles M & Goldstein M. Jr. Multiple spike train analysis. Proc. IEEE, 65:762 -773, 1977.

9. Gerstein GL. & Aertsen AMHJ. Representation of cooperative firing activity among simultaneously recorded neurons. J. Neurophysiol. 54:1513-1528, 1985.
10. Gerstein GL, Perkel DH & Dayhoff JE. Cooperative firing activity in simultaneously recorded populations of neurons: Detection and measurement. J. Neurosci., 5:881-889, 1985.
11. Schneidman E, Berry MJ 2nd, Segev R & Bialek W. Weak pairwise correlations imply strongly correlated network states in a neural population. Nature 440:1007-1012, 2006.
12. Bernard, MR, Zhou, Z & Bonds AB. Synchrony in Cat Visual Cortex is More Selective for Natural Images than Average Firing Rate. AREADNE Conference (Research in encoding and decoding of neural ensembles) Santorini Greece, June 2006.

2.3 Diamond Microelectrodes to Support the Bio-Optic Task

2.3.1 Summary Results

Quantity and quality of signal from the life system source are both essential to data collection success, and depend significantly on the construct of the probes. As described in the proposal, the diamond-coated microelectrodes fabricated thus far are intended to provide more and better signal than metal only needles of previous design. Enough had been learned (2.3 - 1) to realize that the bio-system would be significantly improved if: a) the diamond probes were sharper (to <500nm radius) and b) the isolation of the sheath was better. The fabrication team developed means to achieve this in the first year, including applying nanodiamond film processing to the probes. Specifically, the tungsten needle electrode substrate was coated with nanodiamond film, the tip sharpness <1 micron radius of curvature obtained and the target impedance of ~1M Ohms achieved, see Figure 2.3 - 1. Their electrochemical superiority was clearly demonstrated, Figure 2.3 - 2. A concept design for next generation array of electrodes was established, Figure 2.3 - 3. Further effort on this subtask awaits funding priorities.

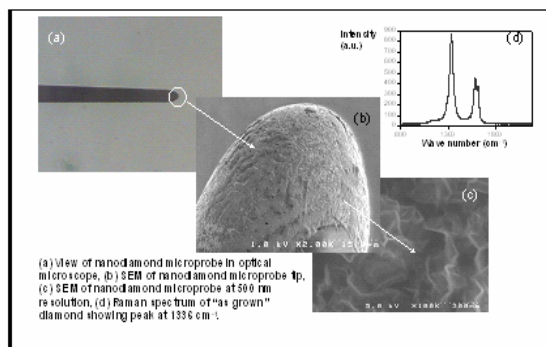


Figure 2.3 - 1 Diamond Bioprobe

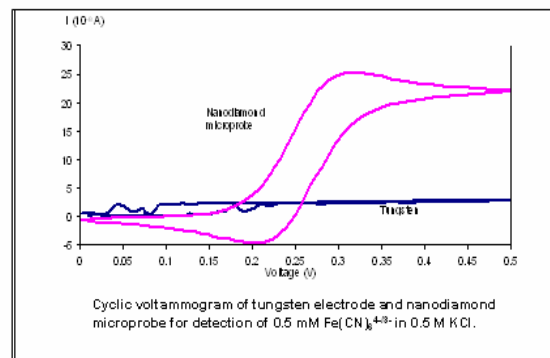


Figure 2.3 - 2 Probe Chemsensor response

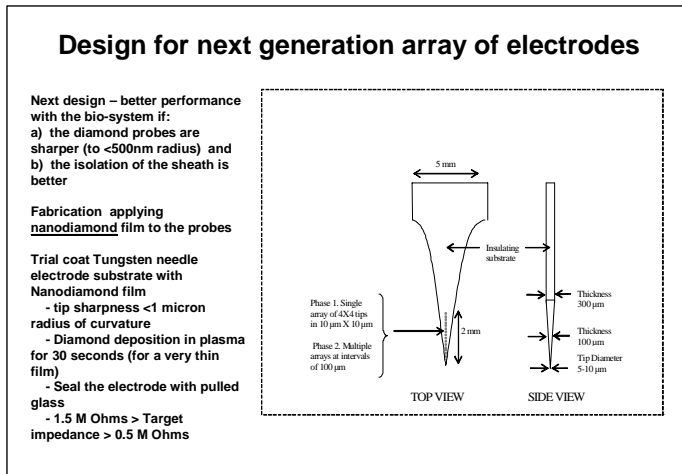


Figure 2.2 - 3 Next Design for Single Diamond Neural Bioprobe

2.3.2 References

1. W. P. Kang, J. L. Davidson, A. B. Bonds, K. L. Soh, S. Basu, and D. E. Cliffel, "Diamond-Derived Electrodes for Electrochemical Analysis", **9th International Conference on New Diamond Science and Technology**, Tokyo, Japan, 2004.

2.4 Develop Advanced IR Display

As part of the CAS Program, Vanderbilt proposed to conduct research with its diamond nanotechnology capabilities for enhancing imaging sensor performance, including advanced high definition infra-red displays. Significant progress to plan, presented below, was achieved.

2.4.1 Background

A need exists for an emitter in the infrared and related frequencies of the spectrum that is efficient, strong, responsive, tunable, miniaturizable, electronically addressable and cost effective. Present technology, which often resorts to "hot wires", an approach more than a century old, is fragile, unreliable, slow and expensive.

Vanderbilt has developed their diamond microfabrication capability to achieve diamond thermal emitters [Ref. 2.4 - 1, 2, 3]. The "glowing" diamond, Fig. 2.4 - 1 can be patterned into a variety of configurations and sizes to achieve robust, efficient, cost effective, high-performance, IR (infrared) or other frequencies emission element by employing Vanderbilt's diamond deposition technology. It is possible to change the frequency in the device very rapidly across a wide range of electronically tunable options and further possible to combine these elements into a pixel array. The necessary elements to achieve this have been demonstrated at Vanderbilt including:

- A. Pattern emitting diamond elements with a monolithic microelectronic interconnect.
- B. Power behavior including emission from deep IR to visible.
- C. Processing capability to achieve emission elements on silicon or ceramic substrates, attached or suspended.

Current-voltage evaluation of the diamond resistors showed that the resistors would experience, due to negative thermal or voltage coefficient of resistance, a region of rapidly rising current flow with increasing voltage which can be used with proper controlling circuitry to control the resistor emission behavior around a "set point", allowing large emission change with a small change in voltage. From this behavior and the properties of diamond which include the highest thermal conductivity, highest binding energy and lowest reactivity of any material known it is an ideal candidate material to serve as an emission source for black body (a.k.a. I^2R , Joule heating) radiation.

The current and power densities observed from these Vanderbilt diamond power resistors are much higher than any other material. For example, a sample sustained 24.6 W. Its cross sectional area was $1.98 \times 10^{-6} \text{ cm}^2$. This yields a power density of 12.4 MW/cm^2 compared to a power density $> 100X$ smaller for Ruthenium Oxide, a common power resistor material. In rough comparison, a light bulb filament operates at $\sim 50 \text{ kW/cm}^2$. The average power sustained by a typical diamond microresistor was approximately 13 W. Current densities were observed as high as $\sim 9 \times 10^4 \text{ A/cm}^2$.

The technology transfer/commercial ramifications of this technology can be seen from this following short list from the many possible applications:

- A very fast digital "TV screen" in the IR, used for biomedical illumination or mapping, security monitoring, and combat/weather/medical image simulation.
- The diamond emitter will be a very unique illumination source for *chemical analysis*. Many analytical instruments for environmental quality monitoring (air, water, factory effluent, automotive standards, etc.) for food processing, pharmaceuticals, biological fluids (blood, plasma, etc.), oil refining {anywhere that the substances involve organic (Carbon-Hydrogen) materials} use an IR beam to illuminate, stimulate, or otherwise analyze known and unknown samples.
- The printing/copying process - an array of these IR elements, at the microsize achievable with this technology, could significantly alter the cost and size aspects of the entire thermal printing industry.

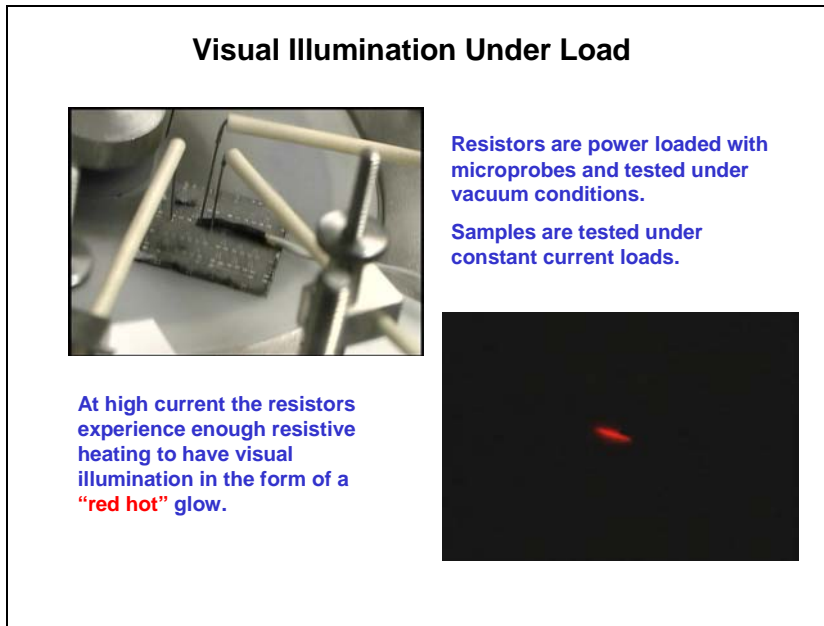


Figure 2.4 - 1 Diamond Resistors Glowing Under Load

Cost considerations: because diamond element fabrication is from a simple CVD process and from inexpensive materials (methane and hydrogen), the IR elements can be produced as cheaply as conventional microelectronic structures such as chip resistors. Also, the ruggedness of diamond emitters eliminates the requirement of a "bulb" configuration sometimes encountered in present applications.

2.4.2 Results

2.4.2.1 Overview

The first year, just completed and the subject of this report, had the objective of design of a diamond IR emitting element (as per Milestone Three in the proposal document - The prototype diamond IR pixel element will be designed in the first year.). Conduct research with Vanderbilt nanotechnology capabilities for enhancing imaging sensor performance, including establishing design approach for advanced high definition infra-red displays.

Objectives for the second year and beyond, are fabrication, characterization, design optimization and operating limit evaluation of diamond pixel element IR array and research nanotechnology capabilities for diamond based IR pixels, including construction of prototype advanced high definition infra-red displays for enhanced imaging sensor performance. In subsequent years, the design and process will be further developed and characterized, the element performance evaluated for limit behavior. Preliminary design for a multi element array will be achieved and fabrication and characterization will be performed in year 2 to 3.

2.4.2.2 Project Performance

The process masks for IR pixel elements were prepared. Fabrication of the prototypical diamond micro-resistor pixel was conducted *ahead of plan*. The instrumentation system for their dynamic evaluation was configured and preliminary testing performed *ahead of plan*.

Freestanding diamond resistors were determined to be the appropriate configuration for the project objectives. Investigation of their electrothermal properties became a planned action. A freestanding resistor has a high thermal resistance between the resistor and the substrate due to the cavity and leads to a higher temperature of the resistor relative to the substrate (2.4 – 4-7). This temperature gradient can then be sensed. The suspended resistor architecture is thermally isolated and appears as a point heat-source (2.4 - 8). Thus the freestanding diamond resistor we are developing will be superior to present technology using resistive arrays.

2.4.2.4 Fabrication

Figure 2.4 - 2 shows the composite mask of the test resistors, cavity and metal terminals. The red is the mask area for the actual necked diamond resistors. The green area is for the cavity mask designed for the oxide sacrificial layer. The blue area is the metal masks for the gold contacts. Three different size structures were built. The resistors were designed to have a ‘necking’ pattern to enhance and concentrate the current flow through the resistor body. (Scale-the largest blue square is 0.8mm on a side).

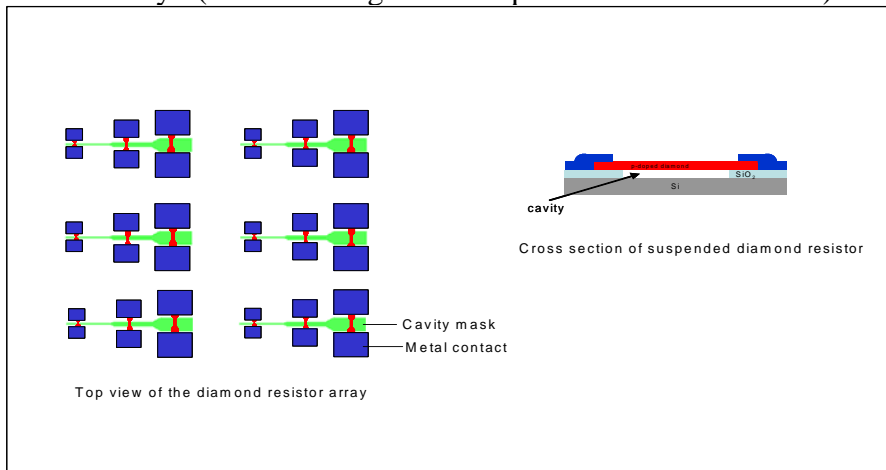
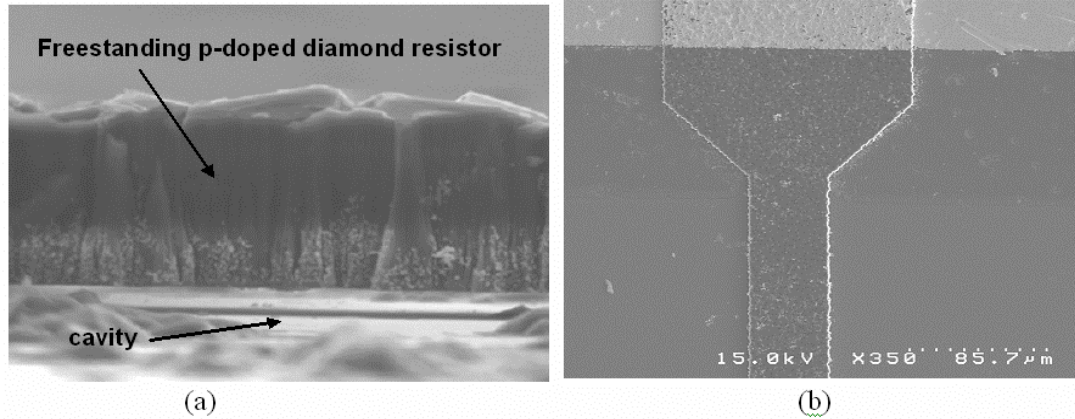


Figure 2.4 - 2 Free-standing diamond resistor mask(left), side view (right)

Freestanding diamond resistors were successfully fabricated; Figure 2.4 - 3 are SEM photographs of the achieved diamond resistors. Polycrystalline diamond films ~ 3 microns in thickness were deposited on an oxidized Si substrate by a plasma-enhanced chemical vapor deposition (PECVD) process. Boron doping was from a trimethylboron (TMB) gas source. A double layer metal consisting of Ti-Au was developed for masking. A thin layer (550 Å) of titanium was evaporated onto the diamond resistor followed by 3000 Å Au forming an ohmic contact. The TiAu layer with low resistance and high melting point is more suited to high power and high temperature applications. The

resistor geometries were achieved in the CVD diamond layer by direct etching in oxygen plasma using a patterned metal mask

Three different prototype resistor structures were fabricated, figure 2.4 - 4 for this study. The resistors were “necked” in shape, as can be seen in the figure, and ranged in length from 50 μm to 200 μm . The necking pattern is designed to enhance and concentrate current flow. The structures were 10 μm to 100 μm in width. Thermally grown SiO_2 of 1 μm was the layer the resistors were on and was the layer removed locally to form a cavity under the diamond resistor around the neck area.



**Figure 2.4 – 3 (a) SEM of freestanding diamond resistor (side view,4500 x),
(b) SEM of resistor neck area (350 x)**

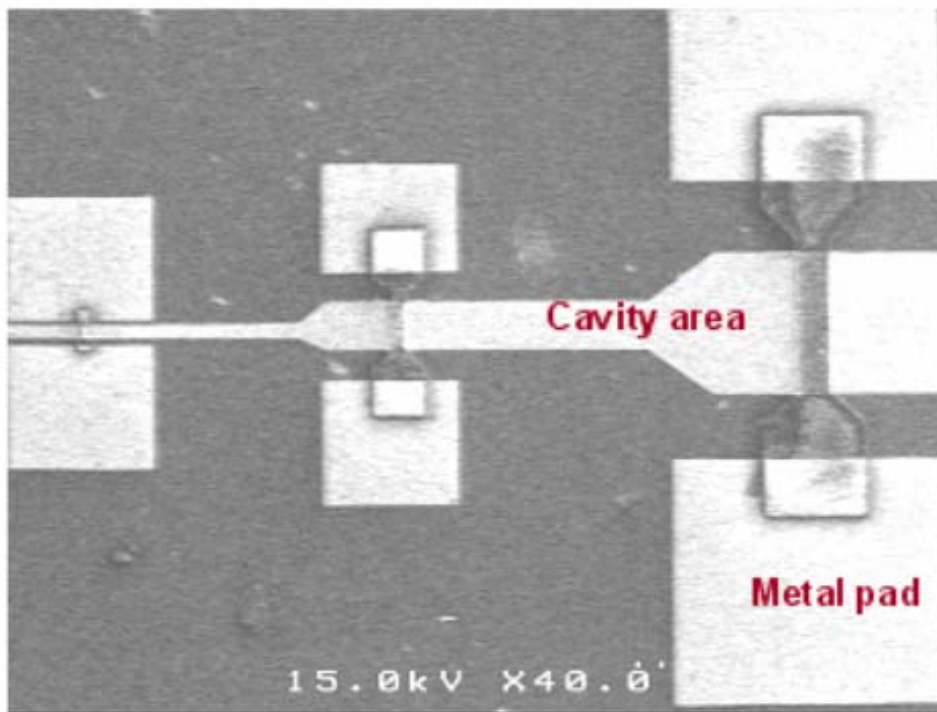


Figure 2.4 - 4 Three Different IR Pixel Resistors (R)

2.4.2.4 Testing

Characterization of the Microstructures; Current Pulse Heating, the intent is to characterize the thermal response/thermal properties and *dynamic* response (*e.g.* sensitivity, frequency, and dynamic range) of the suspended diamond resistor in responses to an impulse power load, see Figure 2.4 - 5. A resistor will be rapidly heated from a powerful current pulse generator while the voltage drop and the current are measured simultaneously. The diamond resistor responds faster to a step function in heater current than other materials (2.4 - 9) and this will be quantitatively measured.

The resistors were subjected to current-pulsed heating for evaluation and characterization. A controlled current pulse was generated using a Magnavolt™ High Voltage DC Power Supply/Pulse Generator. A data acquisition computer running LabView™ software regulated the frequency and duty cycle of the pulses. A low level TTL pulse was generated by the computer and used as the control signal for the pulse generator. In this configuration, the pulse generator could deliver a large controlled output (0-5000V, 0-5A) to the load up to 1kHz. Various pulse magnitudes and durations were used. Due to the small geometries of the freestanding resistors, contact probes were located in close proximity. Tests were conducted in vacuum, $\sim 5.8 \times 10^{-5}$ Torr, to reduce atmospheric ionization and subsequent electrical arcing between the probes. The current profile of a typical freestanding resistor is shown in Figure 2.4 - 6 when the resistor was subjected to a short pulse at low current.

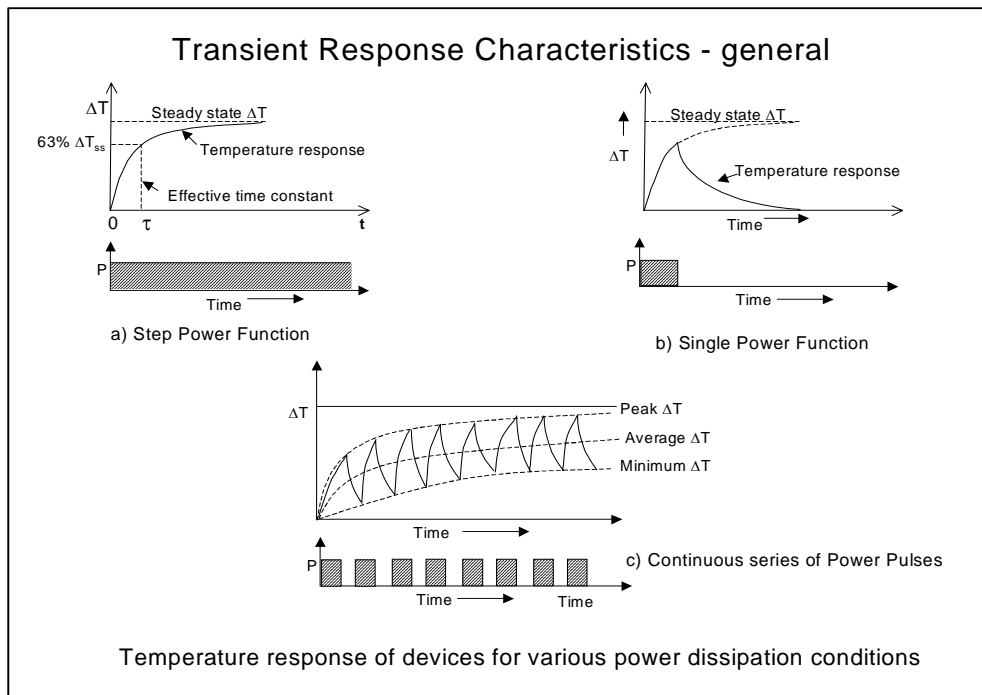


Figure 2.4 - 5 Suspended diamond resistor in response to an impulse power load

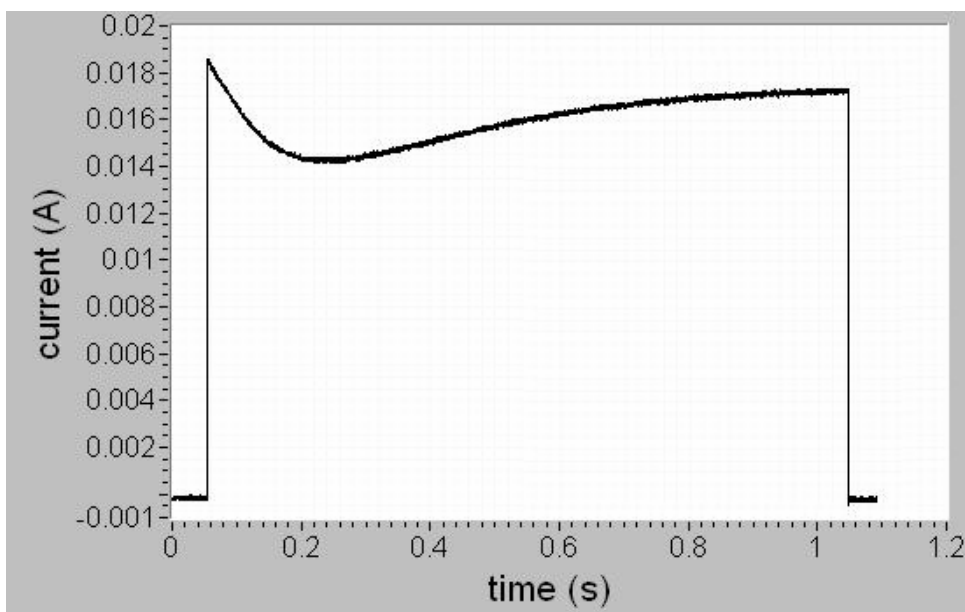


Figure 2.4 - 6 Resistor under low current load (short pulse)

2.4.3 Summary and Plans

The objectives of Year 1 were exceeded. The prototype resistors were designed and fabricated and thermoelectric characterization begun.

In the coming year 2, as per the original proposal and as governed by the level of funding, we will continue to develop the IR pixel device with a focus on:

1. Quantifiably measuring the $T(t)$ response as a $f(I*V, t)$ input to the diamond resistor elements
2. Model thermal response to physical and electrical parameters of the microresistor element and its surroundings. Specifically, as regards resistor characterization, because we have now successfully begun to characterize their electrical behavior under pulse heating, a method of quantifying the thermal luminescence of the resistors is needed.
3. Refine fabrication processes with eye toward array construction for a simple display (addressable elements).

2.4.4 References

1. J. Davidson, W. Kang, K. Holmes, A. Wisitsora-At, P. Taylor, V. Pulugurta, R. Venkatasubramanian and F. Wells. "CVD Diamond for Components and Emitters", *Diamond and Related Material*, 10, pp. 1736-1742, 2001
2. K.C Holmes, "Piezoresistive Micro-Electro-Mechanical Applications in Diamond Films", Doctoral Thesis Dissertation, Vanderbilt University, December 2002.
3. Puteri S. M. Hamari, Patrick Taylor, Kevin C. Holmes, J.L. Davidson and W. P. Kang, "Construct and Properties of Microelectronic Diamond Resistor", High Temperature Electronics Conference, HITEC 2004, Albuquerque, NM, May 2004
4. Charlot, B. *et al*, (1989), TIMA Lab Research Reports, "Fault Simulation of Thermal MEMS", http://tima.imag.fr/publications/files/rr/fst_89.pdf
5. Kim, K and Satche, (1991)W. "Dynamic fracture test of metal thin films deposited on an insulating substrate by a high current pulse method", *Thin Solid Films*, 205, 1991, p. 176-181.
6. Richard G. Lane, "Innovations in Infrared Scene Simulator Design", Santa Barbara Infrared Inc. <http://www.sbir.com/pdf/innovations.pdf>
7. Charlot, B. *et al*. TIMA Lab Research Reports, "Fault Simulation of Thermal MEMS", http://tima.imag.fr/publications/files/rr/fst_89.pdf
8. M.Parameswaran, R. Chung, M. Gaitan, R.B. Johnson and M. Syrzcki, "Commercial CMOS Fabricated Integrated Dynamic Thermal Scene Simulator", IEEE, Electron Devices Meeting, 1991. Technical Digest., International 8-11 Dec. 1991, Page(s):753 – 756].
9. Roppel, T., *et al*, (1992), "Thin film diamond microstructure", *Thin Solid Films*, 212, 1992, pg. 56-62.

3.0 UAH-CAO High Speed Wavefront Sensor Final Report

The goal of this research effort was to establish a testbed to analyze and advance a high speed wavefront sensor concept. The concept, based around a pair of Fourier Transform Lenses (FTL's), requires a high quality optical system and the appropriate filter functions. In this effort, a high quality FTL design was completed, utilizing commercial off-the-shelf optics, and the codes were developed to model, design, analyze and produce the necessary filters. Additionally, the means for producing the filters through two methods were completed; amplitude-only filters by simple printing techniques, and phase-holographic filters. Thus, the goal of the effort, to develop the testbed upon which these high-speed wavefront sensors can be analyzed and advanced, was accomplished. Additionally, a new method of designing apochromatic hybrid lenses was derived, and an approach for transitioning custom lens designs into COTS lens systems has been successfully tested.

3.1 The High Speed Wavefront Sensing System Concept

3.1.1 Basic Configuration

The high speed wavefront sensor to be advanced is based on the physics of Fourier Optics, more specifically, analogue optical computing. Analogue optical computing is based on the inherent property of a lens to produce a Fourier spectrum at the back focal plane of the lens given an input complex wavefront[1]. Thus, given the complex input function \mathbf{s} , the back focal plane contains the Fourier 2-D Transform of the input, $\mathbf{S} = \mathcal{F}\{\mathbf{s}\}$. As shown in Fig. 3.1, by inserting a complex optical structure in this plane, an optical filter with a complex transmittance defined by the function \mathbf{H} , one can manipulate the input object's spectrum for a variety of results; discrimination, tracking, image processing.

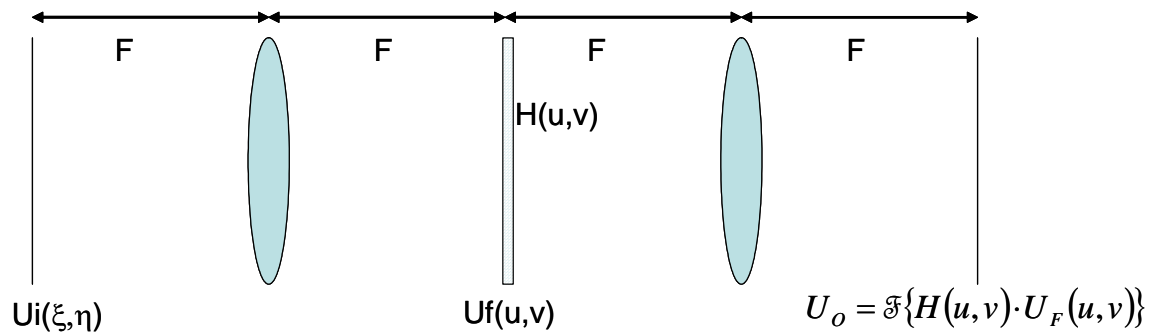


Figure 3-1. Basic layout of the high speed wavefront sensor.

The wavefront which has transmitted through the filter is now the pure multiplication of the incident wavefront, \mathbf{S} , and the filter function, \mathbf{H} . Allowing this new wavefront, $\mathbf{H} \cdot \mathbf{S}$, to propagate through a second Fourier lens yields the convolution of the original input, \mathbf{s} ,

and the impulse response of the filter, **h**. The careful definition of the filter and the geometry of the final Fourier Optics leg of the system define how the wavefront errors will be sensed. The properties of the fabricated filter, essentially a diffraction grating, can be further optimized to enhance sensitivity to individual aspects of the input, or to provide multiple effects from a single element.

This high speed wavefront sensor system is based on the concept of an analogue optical computer whose matched filters are, in a sense, Point Spread Functions for the wavefront errors we intend to detect. As an example, we assume the wavefront entering the system has a pure defocus phase error,

$$U(x, y) = U_0 e^{j \frac{2\pi}{\lambda} (x^2 + y^2) \mathcal{W}_{020}},$$

where \mathcal{W}_{020} is the magnitude of that error and has units of [1/length]. If one of the phase functions the filter system is trying to detect this power error, then one could immediately define the filter as the complex conjugate of that phase function,

$$H(\xi, \eta) = e^{-j \frac{2\pi}{\lambda} (\xi^2 + \eta^2) \mathcal{W}_{020}},$$

such that when the two are multiplied at the Fourier plane, they will yield an unaberrated wavefront which, after passing through the second Fourier optics leg, will yield a diffraction limited PSF. By looking at the peak intensity of the PSF, by placing a pinhole at the PSF followed by a single detector or by using a detector array, one could measure whether the wavefront is corrected. However, this particular detection scheme is quite limited. As defined, it will only match a single magnitude of power, and crudely indicate deviation from that power[2,3].

If, in addition, we introduce a linear phase shift, \mathcal{W}_{001} , to the defocus function and then fabricate the filter such that several diffracted orders, n , are generated, we can now place several detector systems at the output of the second Fourier optics leg, each one tuned to one of the following filter functions:

$$H(x, y) = \sum_n e^{-j \frac{2\pi}{\lambda} [(x^2 + y^2) \mathcal{W}_{020} + \mathcal{W}_{001} \cdot x] n}$$

Each diffracted order will be tuned specifically to detecting the phase where n is a positive or negative integer. Thus, each channel of this sensor will be optimally tuned for integer multiples of the base defocus error, and the output for the various orders will be physically separated at the output of the system. By appropriately wiring the output of all the detectors, an analogue circuit which calculates arbitrary defocus with higher accuracy could readily be designed.

3.1.2 New System Architectures

Concept 1: The Selectable Wavefront Sensor Approach

The complexity of designing filters and producing filters is driven by how many simultaneous functions each filter must provide. Although we have shown that a simple

amplitude filter which will accommodate several filter functions can be produced, and that more complicated grating functions can readily be designed, the testbed we are producing has the additional ability to accommodate multiple identical beamlets, each of which can address an independent filter function in the filter plane. This approach, which is discussed fully in the Q5 Report and shown in Fig. 3.2, was verified through an optical model that was produced in order to evaluate the required specifications for the filter functions.

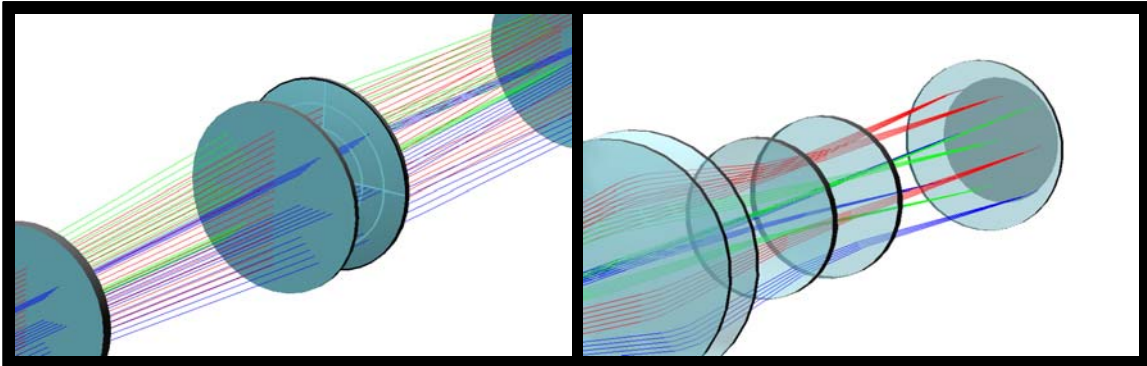


Figure 3-2. Beamlets at the filter plane (left) and at the detector after encountering the array of filters. Note that 9 beamlets (separated into 3 groups red, green and blue) are mixed at the detector plane.

The CodeV model mimics the behavior of the Wavefront Sensor System testbed operating in the Page Oriented Holographic Memory (POHM) form. A single PSF is injected into the first FTL through a grating which splits the converging beam into multiple beams separated by angle. This kind of beam splitter is extremely common and commercially available, often called a fan out grating. Thus, each beamlet will pass through the first FTL and intersect the filter plane at physically separate locations. Now, at each location, a different filter can be encoded with a different linear shift to alter the location of the detection spots. Each identical beamlet is incident on a different region of the filter plane and, hence, a different filter function. Each filtered beamlet is directed to a different location on the detection plane. The advantage of this new configuration is that each filter function can now be produced with a spatial light modulator (SLM) which allows for active selection of what aberration functions are being detected. One can leave a few filter functions fixed, and vary the rest to detect either specific magnitudes of aberration functions or vary the type of aberration function being detected.

Although we have not implemented this approach yet, we believe we have an active reflective SLM in the lab which we hope to use in conjunction with a set of fixed filters. Ultimately, we intend to evaluate such a system and publish our results.

Concept 2: The Non-discreet Wavefront Sensor Approach

A completely different approach utilizes a single filter at a single order to determine arbitrary amounts of aberration, such as defocus. This approach requires a coordinate transformation on the incident wavefront which, for example, remaps the field from an

(x, y) Cartesian mapping to a (ρ, θ) Cartesian mapping. In addition, the (ρ, θ) mapping can be modified to be a (ρ', θ) mapping such that the phase function redistribution yields a linear phase shift in 1-D. Thus, the filter function is now given by the equation

$$H(\xi, \eta) = e^{-j\frac{2\pi}{\lambda} \cdot \xi \cdot W'_{020} \cdot \xi_{MAX}}$$

where we maintain the coordinate notation in the filter plane. We now optically produce an identical coordinate transformation on the input wavefront and send this modified wavefront into the wavefront sensor. At the filter plane, the multiplication of the incident field and the filter function yields

$$U_2(\xi, \eta) = e^{-j\frac{2\pi}{\lambda} \cdot \xi \cdot \xi_{MAX} \cdot (W_{020} - \mathcal{W}_{020})}$$

which means that the magnitude of defocus can be read out at the end of the system on a single position sensing detector (PSD):

$$I(u, v) \propto F\{U_2\} \propto PSF_0(u + \xi_{MAX} \cdot (W_{020} - \mathcal{W}_{020})\lambda \cdot F_2, v)$$

where F2 is the focal length of the second Fourier optics leg. So, the filter function now detects an arbitrary amount of focus error by producing a linearly dependent voltage variation from a single detector.

The challenges increase as one increases the number of aberration types to detect. One either desires filters whose channels produce results that are immune to confounding inputs, or a system whose circuitry can extract the correct output. We have begun to examine this system's level question with the MatLAB tools we have developed, as discussed in the Q4 Report. Preliminary results are indicating that the orthonormality of input functions is maintained after coordinate transformations.

Additionally, we have already begun to process of designing the coordinate transformation optics using diffractive surfaces. Bryngdahl[4] published some of the seminal work in this area. Two of the researchers here at UAH have had previous experience performing similar analyses and some preliminary designs have been completed.

3.2 The FTL Optics

3.2.1 Design Theory

The basic foundation of the High Speed Wavefront Sensor is the optical decomposition of the wavefront via Fourier Transform. Thus, the design of the optical system which produces the Fourier Transform is paramount. As such, the underlying theory for the optical design had to be well understood in order to ensure that the critical parameters were accounted for, but that negligible parameters did not affect the effort. Thus, we applied a simple yet powerful technique for laying out and evaluating optical systems, the Y-Ybar diagram[5]. Once this framework was developed, a method of chromatic aberration correction for this complex system was applied in a new manner, yielding some powerful approaches for optical system achromatization with hybrid refractive-

diffractive lenses. Finally, a monochromatic design study began, initially yielding an all custom-optic lens design which was successfully transitioned to a significantly less expensive all commercial off-the-shelf design. The final design was determined to have relatively loose tolerances and, as it turns out, to be adaptable to a broad range of wavelengths and still diffraction limited.

3.2.1.1 Paraxial methods – the Y-Ybar Diagram

The design of an FTL must have sufficient aberration correction to both bring plane waves to diffraction limited focus and the convert point sources into diffraction limited plane waves. As discussed fully in the Q1 and Q2 Reports, the optical system must therefore be well behaved at two conjugates simultaneously, and these two conjugates could not be more different; object at infinity versus image at infinity. By laying out the system paraxially, it is apparent that it must have neither image aberrations nor pupil aberrations. Fortunately, a simple approach exists to attack both of these design requirements; make the FTL symmetric about its center. In this way, designing the lens to have no image aberrations simultaneously corrects pupil aberrations.

Another researcher at UAH, Dr. Lloyd Hillman, had developed a new linear algebra approach to evaluating image and pupil aberrations, and exploring how they are connected, through rotations of traces on the Y-Ybar diagram. Dr. Hillman passed away in May of 2005 before he was able to publish this work. Fortunately, a student was working on a Masters degree looking at higher order aberration terms, and much of the work was documented after Dr. Hillman's death in the students' thesis. Several researchers here at UAH intend to publish this work, and the application of his theories is extraordinarily well suited to the design of FTL's. The aberrations of the whole FTL is identical to the aberrations of one half of the design plus an identical lens rotated 90 degrees about the origin. This approach shows great promise for defining what aberration terms are critical at which portion of the optical train, thus guiding the design to its optimum configuration.

3.2.1.2 Addressing Chromatic Variations

Initially, the optical design effort began by considering a broad waveband system. Defining what signifies achromaticity for this system coupled to the fact that the filters were initially going to be diffractive, it was anticipated that designing the appropriate system would require a hybrid diffractive-refractive lens system. Thus, a new application of a powerful color-correction approach, the Buchdahl Chromatic Coordinate[6,7], was derived and applied, as discussed in the Q1, and Q2 Reports. The Buchdahl Chromatic Coordinate has been successfully used to design achromats and apochromats from standard available glasses and liquids. The extension of the approach to diffractive systems has not been employed until now.

Buchdahl's chromatic coordinate defines the dispersion of a material by first making the transformation from wavelength, λ , to the unitless variable $\omega(\lambda)$,

$$\omega(\lambda) = \frac{\lambda - \lambda_0}{1 + \alpha \cdot (\lambda - \lambda_0)}, \quad (3.5)$$

where λ is given in micrometers, λ_0 is the center wavelength, and α is an experimentally determined value which, for $\lambda_0=0.574\mu\text{m}$, $\alpha=2.5$. Following this transformation, the refractive index of a material can be represented by the equation

$$n(\omega) = N_0 + \nu_1 \cdot \omega + \nu_2 \cdot \omega^2 + \nu_3 \cdot \omega^3 + \dots + \nu_i \cdot \omega^i. \quad (3.6)$$

Thus, the refractive index is now a simple polynomial expression with the index at the center wavelength equal to N_0 , and the i th order dispersion coefficient equal to ν_i in Buchdahl's coordinate space. The simplification afforded by the Buchdahl's chromatic coordinate is that the refractive index of a material can be well represented by a low-order polynomial function; typically the second order form is sufficient for finding new apochromatic lens forms.

The dispersion of a diffractive lens is purely a function of the grating law, thus, its power is directly proportional to the wavelength,

$$\phi(\lambda) = \phi_0 \frac{\lambda}{\lambda_0}. \quad (3.7)$$

By solving Eq. 3.5 for the wavelength, λ , and combining it with the equation for the power of a diffractive lens yields the relation

$$\phi(\omega) = \phi_0 \cdot \left[1 + \frac{\omega}{\lambda_0 \cdot (1 - \alpha \cdot \omega)} \right]. \quad (3.8)$$

Expanding this out in a Taylor series of order I about $\omega = \omega(\lambda_0) = 0$ yields

$$\phi(\omega) = \phi_0 \cdot \left[1 + \frac{\omega}{\lambda_0} + \frac{\alpha \cdot \omega^2}{\lambda_0} + \frac{\alpha^2 \cdot \omega^3}{\lambda_0} + \frac{\alpha^2 \cdot \omega^3}{\lambda_0} + \dots + \frac{\alpha^{I-1} \cdot \omega^I}{\lambda_0} \right] \quad (3.9)$$

By equating the bracketed portion of this equation to the Buchdahl equation of refractive index, Eq. 3.6, the coefficients of the dispersion can be computed as

$$\nu_i = \frac{\alpha^{i-1}}{\lambda_0} \quad (3.10)$$

and

$$N_0 = 1. \quad (3.11)$$

Thus, $\nu_1 = 1.74$, $\nu_2 = 4.36$, and $\nu_3 = 10.9$, values which are approximately 2, 3, and 4 orders of magnitude larger than the respective coefficients calculated for typical refractive materials.

Using these terms, one can find the power distribution for a refractive – diffractive hybrid achromat. Following Robb, et. al., the power (linear approximation) of the refractive and diffractive elements are

$$\phi(\lambda_0) = \frac{\nu_{1diff}}{\nu_{1diff} - \eta_1} \phi_t(\lambda_0), \text{ and } \phi_{diff}(\lambda_0) = \frac{-\eta_1}{\nu_{1diff} - \eta_1} \phi_t(\lambda_0) \quad (3.12)$$

The above equations can be applied to finding the power distribution for a hybrid lens with the refractive portion made of the glass SF9.

$$\eta_1 = \frac{\nu_1}{N_0 - 1} = \frac{-0.10603}{0.655847} = -0.16167 \mu m^{-1} \text{ and } N_0 = 1.655847$$

For the diffractive lens, the standard method requires the Abbe number and the new approach requires the first order BCC coefficient. We used wavelengths F (486.1nm), d (587.6nm), and C (656.3nm).

$$V_{diff} = \frac{587.6}{486.1 - 656.3} = -3.4534; \quad \nu_{1diff} = \frac{1}{\lambda_d} = \frac{1}{0.5876} = 1.702 \mu m^{-1}$$

We define an achromat of total power $\varphi_t = 1.0$.

1) Standard method:

$$\varphi = \frac{-V}{V_{diff} - V} \varphi_t = \frac{-33.65}{-3.45 - 33.65} = 0.907; \quad \varphi_{diff} = \frac{V_{diff}}{V_{diff} - V} \varphi_t = 0.093$$

2) Buchdahl's coordinate:

$$\varphi = \frac{\nu_{1diff}}{\nu_{1diff} - \eta_1} \varphi_t = \frac{1.702}{1.702 + 0.16167} = 0.913; \quad \varphi_{diff} = \frac{-\eta_1}{\nu_{1diff} - \eta_1} \varphi_t = 0.087.$$

Thus, the solutions using the standard approach, Abbe number, and the Buchdahl Chromatic Coordinate yield comparable results whose differences are expected, given the process each uses. One finds that the residual axial power is comparable for the two solutions, the primary difference being the location of the crossings. Note that the focus shift for comparably powered pure refractive and pure diffractive solutions is 0.028mm and 0.3mm, respectively, versus the hybrid's 0.003mm.

Where the power of the approach becomes apparent is when the number of refractive elements is increased to 2, and the number of chromatic focal crossings is increased to 4. For thin lenses in contact, a method to both select the best two glasses and to set the power distribution falls out of the derivation. This method has been documented, along with the Buchdahl Coordinate coefficients for a diffractive lens in a paper which is being re-edited for submission to Optical Engineering, and in the Q2 Report. In addition, a variation of this visible waveband analysis, applied to refractive-diffractive hybrid lenses operating in the IR, was presented at the SPIE DSS conference in Orlando, Session 6206 as "Applying the Buchdahl dispersion model to infrared hybrid refractive-diffractive achromats," by Pi, Y. and Reardon, P.J.

3.2.2 The Final Design

A number of preliminary diffraction limited designs were developed which were then exercised to evaluate the aberration space around the design solutions. Both the entrance pupil diameter (EPD) and the field-of-view were expanded, individually and in tandem, to see what form the lenses would be driven to, which is discussed more fully in the Q1 Report. It was found that increasing the EPD lead to significant amounts of higher-order spherical aberration, but it was compensated by the lower-order spherical aberration and slight defocus. This design would have significantly tighter tolerances. When increasing the field, however, the design was primarily limited by Petzval curvature, which is inherent in the form. It was accommodated mostly by defocusing the system which

means that, although still diffraction limited, the image quality is reduced at the center and edge of the field. The tolerances of this design would not be significantly tighter than the base design.

The initial optical design for the final FTL system was for an EFL=1000mm, f/10 telecentric system which was presented at the 2nd Quarter Review in October. It consisted of 6 custom singlets for a single FTL. Quotes to fabricate the lenses had been received; \$16k for the lenses for the two systems. We indicated that a COTS design was being pursued to reduce costs. The new design, shown in Fig. 3.3, was completed and discussed in the Q3 Report. The EFL was reduced to EFL=800mm, but the telecentricity and f/10 were retained. The components, all commercial optics, cost ~\$4400 for the two systems, a major reduction in price with no loss in performance and only minor reduction in aperture diameter.

Although this system was designed for 632nm wavelength, the design can be operated as diffraction limited at 514nm and 532nm with only minor adjustment of airspaces.

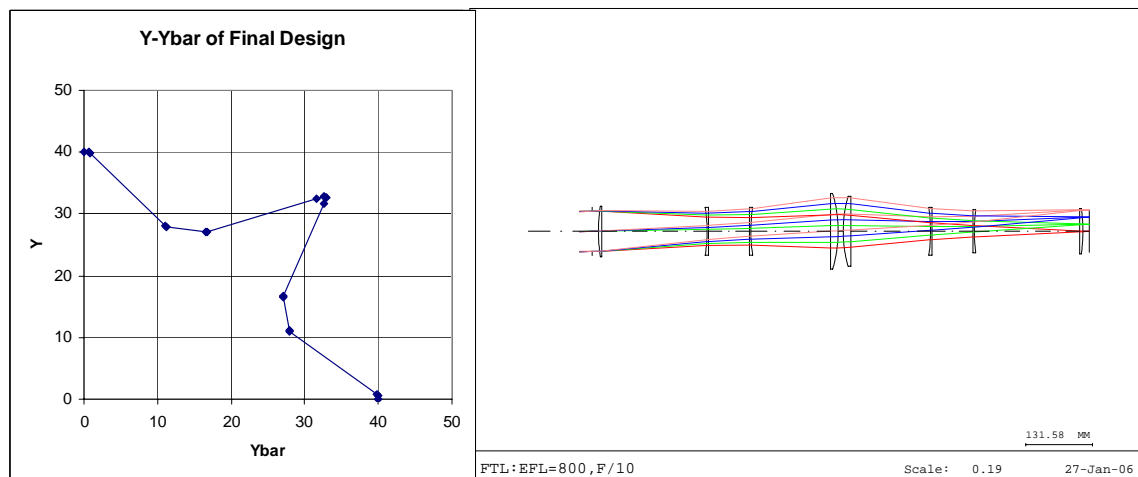


Figure 3-3. Y-Ybar diagram and layout of FTL

As the broad wavelength adjustability indicates, the optical tolerances for the system are extremely loose. For example, 1mm lens thickness errors and 1mm lens separation errors, randomly applied, combine to produce a system which still is diffraction limited, but has a less than 1% change in EFL and a slightly different focal plane location. The radii of the lenses were individually measured, so the design with the actual lens radii were entered into the design code and slightly reoptimized. Thus, even though the sensitivity to radius errors is similarly low, we have very accurate values, essentially eliminating any radius error influence.

This design is phenomenal given its cost and performance. In fact, the Space Bandwidth Product for this FTL system is larger than for any FTL system our team has encountered (over 10^8). We intend to publish this design in Optical Engineering.

Additionally, the COTS lens transition approach utilized in this effort also yielded an extremely cost effective and high quality monochromatic doublet lens. The pairing of an equi-convex and a plano-concave lens can yield a near-zero spherical aberration lens with little coma. Thus, the following two lenses produce a monochromatic doublet of EFL=770mm and EPD=77mm lens with a 20mm diameter diffraction limited image surface, or a 10mm diameter diffraction limited image at EPD=95mm. Comparable achromats are the Edmund Scientific 30976 and the Newport PAC097 which also operate at f/10, but cost ~\$500 and ~\$300 respectively, and are limited to 3" diameter collecting apertures. The Linos 322317 has a 150mm diameter, with great performance, but costs ~\$3600. For comparison, the two lenses we specify in this design study, Fig. 4.3, Ross Optical's L-BCX276 and L-PCC107, costs only ~\$180 in total.

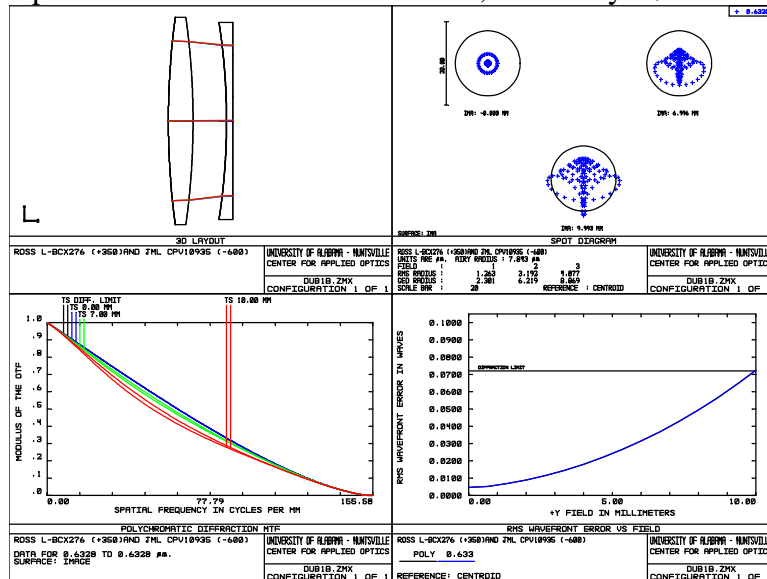


Figure 3-4. Performance of COTS transitioned doublet.

3.3 Filter Implementation

A significant effort was placed on developing the codes to define, model, print and test the filter sets, as is discussed in the Q4 Report. After some efforts to debug the MatLAB algorithms, filters were printed using a standard laser printer, and then optically tested interferometrically and by evaluating the PSF's of the filters. The code was verified, and the filters' theoretical performance in Wavefront Sensor System was modeled using additional MatLAB codes developed under this effort. Testing verified the codes and revealed the prints' limitation, but two simple workarounds were conceived.

3.3.1 Design Coding in MatLAB

The required MatLAB code was developed to numerically model the filters. The code was initially directed to model the Zernike Phase functions for Z4 (defocus) and Z7/Z8 (horizontal and vertical coma). The first step was to produce the general codes for producing these phase functions which was successfully completed. This was verified by

quantitative analysis of the data generated in the data tables. As the Wavefront Sensing system is based around a Fourier Transform lens system, coding the Fourier system was done, using a relatively straight forward DFT approach, however, the code was extended to allow for Fresnel or Fractional Fourier transforms. Thus, the “diffraction pattern” or PSF of a lens with the previously coded filter function could be computed and analyzed. The familiar diffraction patterns for defocus and coma resulted. Thus, initially, two code modules were completed.

One implementation for the system is to utilize binary phase-only filters. These filters primarily produce two diffracted orders, ± 1 , with $\sim 40\%$ efficiency for each order. The code had to be modified to accurately represent this new configuration; the continuous phase profile is replaced by steps of 0 or π radians. This unfortunately now places both diffracted orders’ angular spectrums to be essentially parallel, thus their correlations will end up directly on top of each other at the detection end of the system. Binary tilt, or linear phase shift, was applied to the functions to separate the orders. Thus, if the encoded phase filter is a single wave of Z_7 , the filter should produce two outputs, laterally separated in the detection plane; one for $+Z_7$ and the other for $-Z_7$.

To model the output of the Wavefront sensor with the Z_7 detecting filter in place, the model assumed a PSF entering into the system, being Fourier transformed, and then passing through the filter. If a positive Z_7 is incident, the PSF has a peak intensity ~ 6 times that of its complement. Likewise, if the incident beam has negative Z_7 , the negative Z_7 sensing PSF has a peak intensity ~ 6 times that of its complement. If on the other hand, the incident wavefront has pure Z_4 , the output shows no distinction between the two spots, hence, no indication of any Z_7 . Thus, the system will selectively indicate the presence and amount of a specific aberration, within a range defined by twice the magnitude of the encoded of aberrations.

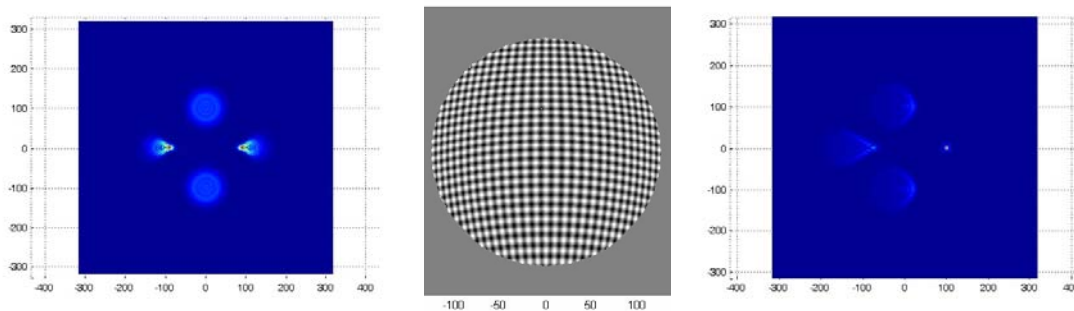


Figure 3-5 From left to right, a filter's impulse response, the filter, and the response of the filter to an input field with $+Z_7$.

In the real wavefront sensing system, one can use multiplexed filters to detect several aberrations simultaneously. To model this, the aberrations for Z_4 and Z_7 were combined into a single filter, as shown in Fig. 3.4, but the linear phase shift was defined to be orthogonal for the two cases. When a Z_4 wavefront error is input into the system, the output clearly indicates its presence and shows no indication of the orthogonal Z_7 error, as expected. Similarly, when a Z_7 wavefront error is input into the system, the output

clearly indicates its presence and shows no indication of the orthogonal Z4 error. Thus, models of the system clearly indicate that the basic Wavefront Sensing concept is feasible.

As the primary goal of this first Years' funding is to develop a test bed and software tools to evaluate new filtering concepts, a simple, rapid and inexpensive way to produce the filter sets is desired. With the prevalence of fairly high-resolution printers, phase functions can be readily and accurately produced as amplitude-only filters. Advantages of this approach include the fact that the filters will, in fact be inherently multi-order, thus each filter will produce spots with several magnitudes of the aberration to be detected. This can be utilized to either expand the dynamic range or the resolution within a fixed range of the Wavefront Sensor. Other advantages are very fast production and very low price. The primary disadvantage is the relative low efficiency as a significant portion of the beam transmits undiffracted, and, depending on the duty cycle of the pattern, the first orders terms range from 10% to 25%. A MatLAB routine was written to correctly design and model these amplitude-only filters.

3.3.2 Filter Testing

Filter testing was critical to verify that the code was, in fact producing the correct phase functions both in scale and form. Two approaches were utilized; the first was to examine the focused spot after a beam propagates through the filter (the impulse response of the filters), and the second was to directly measure the phase with an interferometer.

To directly measure the PSF of a lens system having first passed through the filter, the filters were mounted in front of a collimated HeNe source. For this purpose, a Zygo PTI interferometer producing a 4" diameter beam was used. The beam was then focused by a large diameter focusing lens, passed through an attenuator and onto a Pulnix TM-9701 progressive scan camera at the focus of the lens. The data was grabbed through a National Instruments PCI 1422 frame grabber card using Labview. The data showed that the filters were, in fact, inducing the desired phase errors onto the beam, but there was difficulty separating the orders due to the relative short focal length of the focusing lens, and, therefore, difficulty in seeing many of the orders at the same time. Additionally, the scale of the PSF's were only clearly resolved when the magnitude of the filter function aberration was large enough spread the PSF over many pixels. Even so, it was readily apparent that the spots were as desired when viewed in real time. However, a more quantitative result was desired.

Thus, the approach to utilize a Wyko 400 Fizeau PSI interferometer to directly detect the phase error was implemented. In this approach, the filter was placed in the collimated 4" diameter output of the interferometer, a longer focal length lens was used to bring the light to focus, at which a slit was positioned to pass only a single order at a time. A spherical reference mirror was positioned in the confocal position, so that the light from the passed order would reflect back through the slit, the lens, and again through the filter

At this point, the filter would, in fact, generate another whole set of diffracted orders, each with different magnitudes of the encoded wavefront aberration and each at a different angle. Thus, in order to directly detect each diffracted order's effect required tilting the Wyko's reference flat in order to ensure that the wavefront of interest and the reference wave are "parallel."

This approach allowed us to take a single interferogram as the reference, and then subtract this from the other orders' interferograms to yield their phase function. Subsequent interferograms of the adjacent diffracted orders, containing the desired Z4 or Z7 errors, showed similar phase structure, but by allowing the interferometer software to reduce this function minus the acquired reference into a Zernike decomposition, we saw that the desired filter functions were, in fact, recorded properly onto the transparencies. However, the residual phase errors in the substrate were too large for the filter to function properly. Thus, it was decided to remove this error when the filters are implemented in the Wavefront Sensing System by immersing the transparencies in a liquid gate. This will eliminate the deformations due to surface figure errors in the printouts which are the primary source of the distortions.

3.3.3 Holographic Filter Fabrication Lab

Simple printed amplitude filters have been shown to be of very practical use, but there are limitations to them, primarily efficiency and limited spatial frequency. The design and implementation of many filters can be a costly and slow process when investigating numerous filtering approaches, as this testbed is intended to be used. As a means of providing a more efficient and higher resolution filtering capability, effort was invested in building up the capabilities of a hologram fabrication lab. The lab was assembled almost exclusively with donated optical components which had previously been used in a holography lab. Thus, this is not only an extremely useful addition, but it is very cost effective. The lab is primarily based around an Argon Ion laser operating at 514nm, and dichromated gel for the photosensitive media.

In addition to being able to produce more efficient filters, especially by using the selected orders of the printed amplitude filters, the holographic fabrication allows for the production of aberration correcting holographic elements. For example, the vibrating membrane we ultimately intend to couple into the wavefront generator has some fixed deformations on its surface. By properly writing the hologram, these fixed errors can be removed from the membrane and any intervening optical components.

The ability of writing holograms has been demonstrated at 514nm and now at 632nm. Thus, we are now able to create efficient holographic filters at two wavelengths that can be used in our diffraction limited FTL-based wavefront generator which is readily operated at two wavelengths. These efficient gratings can also be used to produce refractive-diffractive hybrid lens systems in future implementations.

3.4 Conclusion

Our goal of developing a testbed for advancing this new Wavefront Sensor concept has been reached. This program began with a concept and no additional supporting efforts. The from-the-basics optical design approach led to a loosely toleranced diffraction-limited system with a broad wavelength range of operation and a massive space bandwidth product. The MatLAB codes are in-place to design and analyze all new filters and system configurations, as well as producing functional amplitude-only filters. These filters can be utilized to produce more efficient phase-only filters holographically in the hologram fabrication facility. And finally, an expansion of the basic Wavefront Sensor form has been made in two directions. First, the use of multi-order filters allows for either an increase in the wavefront sensor dynamic range or its resolution. Second, applying the POHM approach allows for the use of multiple filters, each potentially containing multiple aberration terms, and each potentially a controllable SLM.

Although we are not receiving further funding through the Center for Advanced Sensors for this research, we intend to continue these efforts and publish further on our findings. We have established a testbed for advancing high speed wavefront sensor and intend to use it.

3.5 Publications and Pending Publications

"Applying the Buchdahl Chromatic Coordinate (BCC) to Diffractive Hybrid Achromats," Reardon, P.J., Pi, Y., Being re-edited. To be submitted to Optical Engineering 9/06

"Applying the Buchdahl dispersion model to infrared hybrid refractive-diffractive achromats," Pi, Y. and Reardon, P.J. . SPIE Proc. 6206 (2006)

"A High-throughput Fourier Transform Lens Design using COTS lenses," Reardon, P.J., Pi, Y., Rogers, T., In progress. To be submitted to Optical Engineering 10/06.

"Transformations OF Aberrations in Optical Systems using matrix methods," Hillman, L.W., Reardon, P.J., GRegory, D., Narayankar, R.A. In progress. To be submitted to Applied Optics 12/06.

"Aberration theory of symmetric Fourier Transform Lenses using the Y-Ybar diagram," Reardon, P.J., Pitalo, S.K., Pi, Y., In progress. To be submitted to Optical Engineering 12/06.

"A High-speed Aberration Selectable Wavefront Sensor," Reardon, P.J., Geary, J.M., Pi, Y., Blackwell, T., In progress. To be submitted to Optical Engineering 11/06.

3.6 References

1. Goodman, J.W., Introduction to Fourier Optics, Ch. 8, McGraw-Hill, New York, NY, (1996).

2. Neil, M.A.A., Booth, M.J., Wilson, T., "New modal wave-front sensor: a theoretical analysis," JOSA, Vol.17, No.6 (2000).
3. Anderson, G., Reibel, R., "Holographic Wavefront Sensor," SPIE Proc. 5894 (2005).
4. Bryngdahl, O., "Geometrical Transformations in Optics," JOSA, Vol. 64, No. 8 (1974).
5. Delano, E., "First Order Design and the y, ybar Diagram," Appl. Opt., Vol.2, No.12 (1963).
6. Buchdahl, H.A., Optical Aberration Coefficients, Dover, NY, (1968).
7. Robb, P.N., Mercado, R.I., "Calculation of Refractive Indices Using Buchdahl's Chromatic Coordinate," Appl. Opt. Vol.22, No.8 (1983).